TECHNICAL UNIVERSITY OF CRETE
SCHOOL OF ELECTRICAL AND COMPUTER ENGINEERING
TELECOMMUNICATIONS DIVISION

Device-free Indoor Localization of People with Radio Frequency

by

Anastasios Kleniatis

A THESIS SUBMITTED IN PARTIAL FULFILLMENT OF
THE REQUIREMENTS FOR THE DIPLOMA OF

ELECTRICAL AND COMPUTER ENGINEERING

THESIS COMMITTEE

Professor Thrasyvoulos Spyropoulos, *Thesis Supervisor*
Professor Aggelos Bletsas
Professor Michail G. Lagoudakis

Chania, July 2024

ΠΟΛΥΤΕΧΝΕΙΟ ΚΡΗΤΗΣ
ΣΧΟΛΗ ΗΛΕΚΤΡΟΛΟΓΩΝ ΜΗΧΑΝΙΚΩΝ ΚΑΙ ΜΗΧΑΝΙΚΩΝ ΥΠΟΛΟΓΙΣΤΩΝ
ΤΟΜΕΑΣ ΤΗΛΕΠΙΚΟΙΝΩΝΙΩΝ

Ραδιοσυχνοτικός Προσδιορισμός Θέσης Ανθρώπων χωρίς Συσκευές σε Εσωτερικούς Χώρους

από τον

Αναστάσιο Κλενιάτη

ΔΙΠΛΩΜΑΤΙΚΗ ΕΡΓΑΣΙΑ ΠΟΥ ΥΠΟΒΛΗΘΗΚΕ ΣΕ ΜΕΡΙΚΗ ΕΚΠΛΗΡΩΣΗ ΤΩΝ ΑΠΑΙΤΗΣΕΩΝ ΓΙΑ ΤΗΝ ΑΠΟΚΤΗΣΗ ΤΟΥ ΔΙΠΛΩΜΑΤΟΣ ΤΟΥ

ΗΛΕΚΤΡΟΛΟΓΟΥ ΜΗΧΑΝΙΚΟΥ ΚΑΙ ΜΗΧΑΝΙΚΟΥ ΥΠΟΛΟΓΙΣΤΩΝ

ΕΠΙΤΡΟΠΗ ΔΙΠΛΩΜΑΤΙΚΗΣ ΕΡΓΑΣΙΑΣ

Καθηγητής Θρασύβουλος Σπυρόπουλος, *Επιβλέπων*
Καθηγητής Άγγελος Μπλέτσας
Καθηγητής Μιχαήλ Γ. Λαγουδάκης

Χανιά, Ιούλιος 2024

Abstract

Device-free localization (DFL) is an emerging technology with diverse applications, including security, customer behavior analysis, and smart buildings. DFL focuses on locating individuals without requiring them to carry devices or actively participate in the localization process. Recent research has leveraged wireless technologies for DFL due to their cost-effectiveness and non-intrusive nature. However, accurately localizing multiple people in an area remains challenging due to severe multipath effects.

This work addresses these challenges by modeling multipath reflections and proposing two DFL methods that utilize additional signal characteristics, such as phase and read rate, unlike existing methods that rely solely on received signal strength. Additionally, it introduces a practical fusion technique to combine different DFL methods, enhancing overall performance. Another key component is the deployment of multiple RFID tags within the area of interest, which function as additional wireless antennas, significantly reducing the overall cost compared to the wireless sensor networks commonly used in the literature.

Real-world experiments demonstrated that the proposed methods can achieve accuracy comparable to state-of-the-art techniques and can even surpass them in certain scenarios. Notably, one of the proposed methods achieves 25% better localization accuracy than an existing method, when localizing three targets. Additionally, combining one of the proposed methods with an existing technique enhances the existing method's performance by 40%, 13%, and 28% in one, two, and three target localization scenarios, respectively. Specifically, using 84 passive RFID tags, the localization error is reduced to less than 36 cm for one target, less than 41 cm for two targets, and less than 96 cm for three targets, 90% of the time.

Περίληψη

Ο εντοπισμός χωρίς συσκευές (DFL) είναι μια αναδυόμενη τεχνολογία με ποικίλες εφαρμογές, όπως η ασφάλεια, η ανάλυση της συμπεριφοράς των πελατών και τα έξυπνα κτίρια. Ο DFL επικεντρώνεται στον εντοπισμό ατόμων χωρίς να απαιτείται να φέρουν συσκευές ή να συμμετέχουν ενεργά στη διαδικασία εντοπισμού. Πρόσφατες έρευνες έχουν αξιοποίησει τις ασύρματες τεχνολογίες για τον DFL λόγω της οικονομικής αποδοτικότητας και της μη παρεμβατικής φύσης τους. Ωστόσο, ο ακριβής εντοπισμός πολλαπλών ατόμων σε μια περιοχή παραμένει πρόκληση λόγω των σοβαρών επιδράσεων πολλαπλών διαδρομών (multipath).

Αυτή η εργασία αντιμετωπίζει αυτές τις προκλήσεις με τη μοντελοποίηση των ανακλάσεων πολλαπλών διαδρομών και την πρόταση δύο μεθόδων DFL που χρησιμοποιούν πρόσθετα χαρακτηριστικά σήματος, όπως η φάση και ο ρυθμός ανάγνωσης, σε αντίθεση με τις υπάρχουσες μεθόδους που βασίζονται αποκλειστικά στην ισχύ του λαμβανόμενου σήματος. Επιπλέον, εισάγει μια πρακτική τεχνική σύνθεσης για το συνδυασμό διαφορετικών μεθόδων DFL, βελτιώνοντας τη συνολική απόδοση. Ένα άλλο βασικό στοιχείο είναι η τοποθέτηση πολλαπλών ετικετών RFID εντός της περιοχής ενδιαφέροντος, οι οποίες λειτουργούν ως πρόσθετες ασύρματες κεραίες, μειώνοντας σημαντικά το συνολικό κόστος σε σύγκριση με τα ασύρματα δίκτυα αισθητήρων που χρησιμοποιούνται συνήθως στη βιβλιογραφία.

Πειράματα σε πραγματικό κόσμο έδειξαν ότι οι προτεινόμενες μέθοδοι μπορούν να επιτύχουν ακρίβεια συγκρίσιμη με τις σύγχρονες τεχνικές και μπορούν ακόμη και να τις ξεπεράσουν σε ορισμένα σενάρια. Ειδικότερα, μία από τις προτεινόμενες μεθόδους επιτυγχάνει 25% καλύτερη ακρίβεια εντοπισμού από μια υπάρχουσα μέθοδο κατά τον εντοπισμό τριών στόχων. Επιπλέον, ο συνδυασμός μιας από τις προτεινόμενες μεθόδους με μια υπάρχουσα τεχνική βελτιώνει την απόδοση της υπάρχουσας μεθόδου κατά 40%, 13% και 28% σε σενάρια εντοπισ-

μού ενός, δύο και τριών στόχων, αντίστοιχα. Συγκεκριμένα, χρησιμοποιώντας 84 παθητικές ετικέτες RFID, το σφάλμα εντοπισμού μειώνεται σε λιγότερο από 36 cm για έναν στόχο, λιγότερο από 41 cm για δύο στόχους και λιγότερο από 96 cm για τρεις στόχους, στο 90% των περιπτώσεων.

Acknowledgements

First and foremost, I would like to express my gratitude to my supervisor, Professor Aggelos Bletsas, for his support and guidance throughout this thesis. I would also like to thank Professor Thrasyvoulos Spyropoulos who stepped in as my official thesis supervisor for formal reasons, due to Professor Bletsas's leave.

I am also grateful to my friends and colleagues at the Telecommunications's lab: Giorgos Andreadis, Dimitris Angelou, Vangelis Giannelos, Giorgos Ntoumparas and Giorgos Papadopoulos. Your help was crucial in completing this work and working alongside you made the time spent in the lab both enjoyable and productive.

To my friends and family, thank you for your constant encouragement and understanding. Your support was essential throughout my studies.

Contents

Table of Contents 7

List of Figures 9

1 Introduction 10
- 1.1 Problem Description 10
- 1.2 Prior Art 11
- 1.3 Introduction to RFID Technology 14
  - 1.3.1 Components of RFID Systems 14
  - 1.3.2 Working Principle of RFID 15
  - 1.3.3 RFID Frequencies and Applications 16

2 Phase Method with RF Propagation 17
- 2.1 Introduction 17
- 2.2 System Model 17
  - 2.2.1 Measurement Model and Static Signal Components Removal 20
  - 2.2.2 Modeling Reflections for Tomographic Imaging 21
- 2.3 Compressive Sensing 22
- 2.4 Application of Compressive Sensing in DFL 24

3 Phase Method with Read Rate 28
- 3.1 Introduction 28
- 3.2 Version 1 28
- 3.3 Version 2 30

4 Fusion Scheme for different DFL Methods 31
4.1 Introduction 31
4.2 Fusion Scheme 31
4.3 Noise Reduction Techniques 32

5 Experiments 33
5.1 Introduction 33
5.2 Phase Disturbances Method Modification 34
5.3 Phase Method I - Regularization Parameter 35
5.4 Localization Images 36
5.4.1 One Target Localization 37
5.4.2 Two Targets Localization 37
5.4.3 Three Targets Localization 38
5.4.4 Fusion of different methods 38
5.5 Noise Reduction 41
5.6 Weights' Scaling Comparison 41
5.7 Clustering 43
5.7.1 k-Means Clustering 44
5.7.2 Expectation Maximization 44
5.8 Number of Tags 45
5.9 Phase Method with Read Rate - Ver. 1 vs Ver.2 46
5.10 Cumulative Distribution Functions 47

6 Conclusions 51
6.1 Conclusion 51
6.2 Future Work 52

Appendices

A Localization images from all tested positions 53

Bibliography 66

List of Figures

1.1 Device-Free Localization 11
1.2 RFID reader (left), antennas (middle) and passive tag (right) . 15

2.1 Multiple humans carrying no devices and several passive RFID tags in the room. 18
2.2 Ellipse Model 21
2.3 Compressive sensing system visualization. 23

5.1 Setup of reader antennas and RFID tags and Link Density. . . 34
5.2 Phase Method I - Regularization Parameter 36
5.3 One Target Localization 37
5.4 Two Targets Localization 38
5.5 Three Targets Localization 39
5.6 Fusion of RSSI Method and Phase Method III (Ver.1) 40
5.7 Noise Reduction Techniques 41
5.8 Weight Scaling Comparison using Phase Method III 42
5.9 Clustering and Location Estimation 43
5.10 Impact of the number of deployed tags. 45
5.11 Phase Method III - Ver. 1 vs Ver.2 CDFs 46
5.12 CDF of the localization error of 1 target using the 5th power for scaling. 48
5.13 CDF of the localization error of 2 targets using k-Means for clustering and the 5th power for scaling. 49
5.14 CDF of the localization error of 3 targets using k-Means for clustering and the 5th power for scaling. 50

Chapter 1

Introduction

1.1 Problem Description

Device-free localization (DFL) is an innovative approach to tracking and monitoring individuals or objects within a designated area without requiring them to carry any sensors or devices. This technology leverages the ambient environment and existing infrastructure, such as Wi-Fi, RFID, or other wireless signals, to detect and localize the presence and movement of people. By analyzing the changes in various signal characteristics and patterns as they interact with physical objects and human bodies, DFL systems can infer the location and movement of individuals.

DFL is particularly useful in scenarios where it is impractical or intrusive to equip individuals with tracking devices, such as in elderly care, security surveillance, and customer behavior analysis in retail settings. Another key advantage of DFL is its ability to preserve privacy, while still providing valuable localization data. Unlike traditional methods that rely on cameras or wearable devices, DFL does not require direct visual or physical contact with the subject, reducing privacy concerns and enhancing user comfort.

In this study, Radio Frequency Identification (RFID) technology is utilized to address the challenge of localizing multiple static humans. This problem is especially difficult and many existing methods perform poorly in multi-target scenarios. Moreover, the task is complicated by the fact that static targets have minimal impact on the environment, leading to measurements with low variance. To tackle these issues, two device-free localization methods are proposed, as well as a fusion technique that combines multiple DFL approaches. Comparisons with previous research conducted under real-world conditions (as illustrated in Figure 1.1) are also presented to evaluate

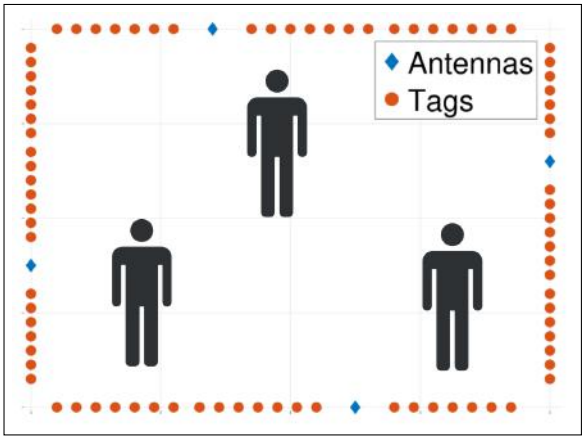

Figure 1.1: Device-Free Localization

the effectiveness of the proposed methods. A shorter version of this work was presented in the "18th Annual International Conference on RFID" [1].

1.2 Prior Art

Device-free localization (DFL) has recently attracted significant research attention due to its diverse applications. Due to the pervasive nature of wireless signals, various technologies, such as Wi-Fi [2], Ultra-Wideband (UWB) [3], and Radio-Frequency Identification (RFID), have been employed in wireless localization studies. Several effective DFL techniques have been developed across these technologies. Specifically, in the case of RFID, there are multiple categories of DFL methods that have been explored.

One prominent category is Radio Vision-based methods, which monitor the shadowing and variations in measurements of different sensor links. Radio Tomographic Imaging (RTI) [4] falls into this category, where the area of interest is surrounded with sensors and the variations of the Received Signal Strength (RSS) are used for target localization. Numerous studies [5–7] have been based on RTI and offer various techniques to improve its performance and eliminate false targets. Histogram-distance [8] and Kernel-distance [9] techniques have also been applied to RTI, which can remove the need for offline measurements.

Another category is based on Radar principles and consists of methods that examine the interaction of wireless signals with the environment and targets, exploiting their scattering or reflection properties. [10–12] have demonstrated potential in modeling human reflections, but have been less effective in multiple targets scenarios. Angle of Arrival (AoA) information is also included in [13] to improve localization, but this system requires at least two readers and multiple antennas, which increase the cost significantly.

Fingerprinting [14] is also a common approach in device free localization. By gathering measurements of a target in multiple locations in the area of interest, a database can be constructed to which new (online) measurements are compared. In [15], a single-target fingerprint database was also used to track multiple targets. These techniques have produced satisfactory outcomes, but the data collection process is time-consuming and requires the topology of sensors to remain constant.

Statistical methods have also been explored in the literature for tracking multiple targets. The use of particle filters in [16] have shown promising results. Their key advantage is that they do not make any assumptions on linearity of the measurement process and do not require the likelihood distributions to be Gaussian. However, they are computationally complex and require a high number of particles to achieve good accuracy.

Additionally, there have been studies focusing on human counting prior to the localization process. For example, in [17], a successive cancellation algorithm was introduced, which counts the number of targets by sequentially removing the effect of each target from the RSS measurements. Through experiments it was shown that it can achieve a counting accuracy of over 80%. Despite this, its application is limited, as it struggles to count and localize more than four subjects successfully, especially if they have overlapping paths.

Although DFL methods using RFID typically rely on RSS measurements, other signal characteristics have also been explored. In [18], phase measurements and read rates are utilized. Significant fluctuations in phase or notable drops in read rate indicate the presence of a target, which is later tracked using particle filtering. Moreover, in [19], Doppler shift changes are employed

to accurately track targets, as they are less sensitive to multipath effects. While these methods show promise, both struggle with tracking multiple targets simultaneously.

Deep learning has recently been applied in DFL with remarkable results. In [20], deep neural networks have been used to enhance the tomographic images that are produced by RSS, phase and read rate measurements, producing clearer and more accurate images. Special neural networks (Autoencoders, Convolutional deep belief networks) have also been used in [21,22] to extract valuable signal features and patterns that could be otherwise be quite complex to model. However, like fingerprinting, large amounts of data have to be collected in order to effectively train these networks and the problem of deploying the trained model in different environments remains challenging.

1.3 Introduction to RFID Technology

Radio Frequency Identification (RFID) is a cutting-edge technology used to automatically identify and track objects, animals, or people. Utilizing electromagnetic fields, RFID systems transfer data between a tag and a reader. With its array of benefits, including cost-effectiveness, energy efficiency, scalability and privacy protection, RFID has become widespread across diverse sectors, such as supply chain management, inventory control, healthcare, and security.

1.3.1 Components of RFID Systems

An RFID system typically comprises three main components: the RFID tag, the RFID reader, and the antenna.

- **RFID Tags**
  - **Passive Tags**: These tags do not have an internal power source. They harvest power from the electromagnetic field generated by the RFID reader and they reflect the signal back to the reader. Passive tags are cost-effective and flexible, but they are more suitable for applications with short range. An example of a passive RFID tag is shown in the right image of Figure 1.2
  - **Active Tags**: Equipped with their own power source, active tags can transmit signals over longer distances. However, they are both bigger and more expensive than the passive tags. They are suitable for applications requiring high read ranges and data transmission rates. They can also have temperature, humidity and other sensors onboard the tag.
  - **Semi-Passive Tags**: These tags have a small internal battery to power the chip's circuitry and thus all of the harvested energy from the reader can be used for communication. In this way, they can achieve longer read distance and higher data transfer rates than the passive tags.

Figure 1.2: RFID reader (left), antennas (middle) and passive tag (right)

- **RFID Readers**

  RFID readers are devices that emit continuous radio waves to activate nearby tags and receive signals back from them. Readers can be handheld or fixed, depending on the application. They are responsible for querying tags and processing the information received. An example of a RFID reader is shown in the left image of Figure 1.2

- **Antennas**

  Antennas facilitate communication between the reader and the tag. The design and orientation of antennas significantly impact the read range and accuracy of the RFID system. The middle image in Figure 1.2 illustrates two such antennas.

1.3.2 Working Principle of RFID

RFID systems operate by using electromagnetic fields to automatically identify and track tags attached to objects. The communication consists of 3 steps:

1. **Tag Activation**: When an RFID tag enters the electromagnetic field emitted by an RFID reader, it gets activated. Passive tags draw power from the reader's field, while active tags use their internal battery.

2. **Data Transmission**: The activated tag transmits its unique identifier and other stored information back to the reader.

3. **Data Processing**: The RFID reader receives the transmitted data and processes it. This data can then be sent to a computer for further processing and storage.

1.3.3 RFID Frequencies and Applications

RFID technology operates at different frequency ranges, each with its own characteristics and applications:

- **Low Frequency (LF)**

  LF RFID systems operate at 125 and 134 kHz. They have short read ranges, typically up to 10 cm, and are used in applications, like animal tracking and access control.

- **High Frequency (HF)**

  HF RFID systems operate at 13.56 MHz. They offer read ranges up to 1 meter and are widely used in applications, such as contactless payment systems, library book tracking, and smart cards.

- **Ultra-High Frequency (UHF)**

  UHF RFID systems operate between 300 MHz and 3 GHz, with typical commercial applications using 860-960 MHz (depending on the region). UHF systems provide longer read ranges and are suitable for supply chain management, asset tracking, and inventory control.

- **Microwave Frequency**

  Operating at 2.45 GHz and above, microwave RFID systems offer very long read ranges and are used in applications, such as toll collection and tracking of large assets.

Chapter 2

Phase Method with RF Propagation

2.1 Introduction

Previous research on RFID localization [23, 24] has demonstrated the significance of signal propagation modeling and accounting for multipath effects. These factors contribute significantly to the accurate localization of RFID tags and even static reflectors within a given environment. A recent study conducted by [10] modeled single bounce reflections from humans within a specific area, leveraging this data for precise device-free localization. In this thesis, this idea is expanded to incorporate multiple types of reflections in a effort to better capture the multipath effect and improve the localization of multiple static humans, which is especially challenging, because of their minimal impact on measurements and the lack of tracking and filtering equations.

2.2 System Model

The received signal in the reader antennas consists of the following components (Figure 2.1):

1. Antenna-tag line-of-sight (LoS) ($a \rightarrow b$).
2. Static environment reflections ($c \rightarrow d \rightarrow e \rightarrow f$).
3. 0th order target reflections ($g \rightarrow h$).
4. 1st order target reflections ($a \rightarrow j \rightarrow h$).

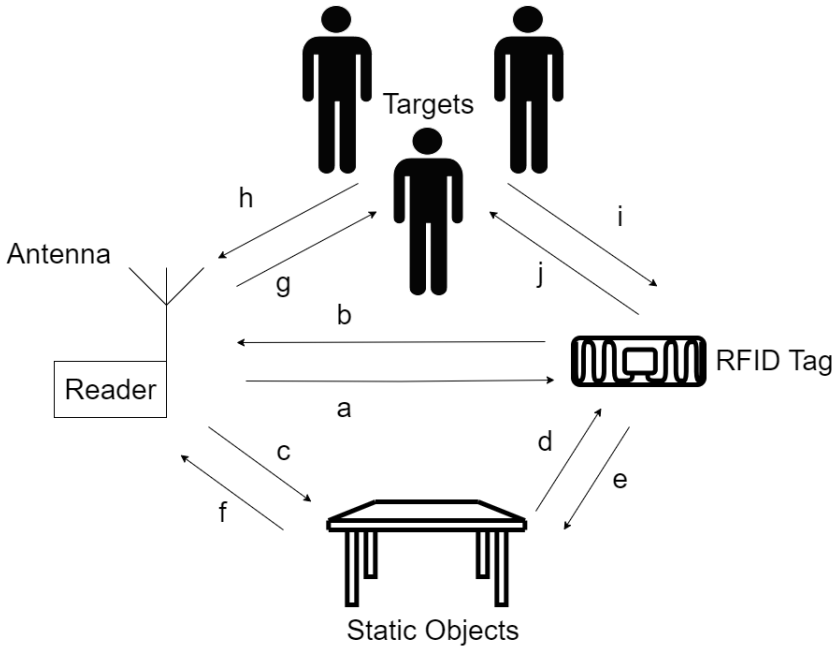

Figure 2.1: Multiple humans carrying no devices and several passive RFID tags in the room.

5. 2nd order target reflections ($a \rightarrow j \rightarrow i \rightarrow b$).

The *large-scale* path loss is modelled as follows:

$$\mathsf{L}_{\mathrm{X}} = \left(\frac{\lambda_f}{4\pi d_0^{\mathrm{X}}}\right)^2 \left(\frac{d_0^{\mathrm{X}}}{d_{\mathrm{X}}}\right)^{v_{\mathrm{X}}}, \tag{2.1}$$

where d_0^{X} is a reference distance and d_{X} is the distance regarding link X (specified at each case, subsequently), λ_f is the carrier wavelength at carrier frequency f and v_{X} is the path-loss exponent. For a free-space or two-ray model, v_{X} takes the value of 2 [25], simplifying the model as follows:

$$\mathsf{L}_{\mathrm{X}} = \left(\frac{\lambda_f}{4\pi d_0^{\mathrm{X}}}\right)^2 \left(\frac{d_0^{\mathrm{X}}}{d_{\mathrm{X}}}\right)^2 = \left(\frac{\lambda_f}{4\pi d_{\mathrm{X}}}\right)^2. \tag{2.2}$$

Antenna m and tag n LoS path at carrier frequency f is modelled as

follows:

$$y_{\text{LOS}}[m,f,n] = \sqrt{2P_c\,\eta\,\mathsf{L}_{mn}\mathsf{L}_{mn}}\; e^{-j2\pi\dfrac{2\,d(m,n)}{\lambda_f}}, \tag{2.3}$$

where $m = 0,1,\ldots,M$, $n = 0,1,\ldots,N$ and $f = 0,1,\ldots,F$.
In addition, P_c is the carrier transmission power at passband, η is the tag power backscattering efficiency[1] and $d(m,n)$ is the distance between reader antenna m and tag n.

Similarly, the 0th order reflections are modelled as follows:

$$y_0[m,f,p] = \sqrt{2P_c\,\eta_p\,\mathsf{L}_{mp}\,\mathsf{L}_{mp}}\; e^{-j2\pi\dfrac{2\,d(m,p)}{\lambda_f}}, \tag{2.4}$$

where $\eta_p \in (0,1)$ the percentage of the signal reflected from the target and $d(m,p)$ is the distance between reader antenna m and target p.

The 1st order reflections are given below:

$$y_1[m,f,n,p] = \sqrt{2P_c\,\eta\,\eta_p\,\mathsf{L}_{mn}\,\mathsf{L}_{np}\,\mathsf{L}_{mp}}\;\times \\ e^{-j2\pi\dfrac{d(m,n)+d(m,p)+d(p,n)}{\lambda_f}}, \tag{2.5}$$

where $d(p,n)$ is the distance of between tag n and target p.

Finally, the 2nd order reflections follow:

$$y_2[m,f,n,p] = \sqrt{2P_c\,\eta^2\,\eta_p\,\mathsf{L}_{mn}^2\,\mathsf{L}_{np}^2}\;\times \\ e^{-j2\pi\dfrac{2\,d(m,n)+2\,d(p,n)}{\lambda_f}}. \tag{2.6}$$

Thus, the received signal is modelled as the superposition of the above

[1]Reflection coefficient η and η_p below, should be modeled as complex and not real, adding a phase term; however, such phase depends on the target material and illuminating direction and is general hard to estimate; thus, reflections η, η_p are modeled as real and their contributing phase can be modeled as additional noise in Eq. (2.7).

components, accordingly:

$$\begin{aligned} y[m,f,n,p] = y_{\text{LOS}}[m,f,n] + y_0[m,f,p] + y_1[m,f,n,p] \\ + y_2[m,f,n,p] + w[m,f,n], \end{aligned} \tag{2.7}$$

where $w[m,f,n]$ is the noise at the receiver.

2.2.1 Measurement Model and Static Signal Components Removal

The received signal is calculated as follows:

$$\boldsymbol{y} = \boldsymbol{\mu} \odot e^{-j\boldsymbol{\phi}}, \tag{2.8}$$

where $\boldsymbol{\phi}$ denotes the phase measurements vector, $\boldsymbol{\mu}$ denotes the received signal strength indicator (RSSI) measurements vector whose values are converted to amplitude units, $y[i]$ corresponds to the measurement of tag n from reader antenna m at carrier frequency f, indexed by $i = (m-1) \times F \times N + (f-1) \times N + n$ and $\odot$ denotes the Hadamard product.

Signal components 1 and 2 (as defined in Section 2.2, referring to antenna-tag LoS and static environment reflections) can be eliminated by using measurements taken in the area of interest when no target is present. During a brief offline phase lasting a few minutes, data is collected when the room is unoccupied ($\boldsymbol{y}_{\text{empty}}$). Later, in the online phase when humans are present, these offline measurements are subtracted from the real-time measurements ($\boldsymbol{y}$). In addition, the one way Line of Sight is removed by dividing with a complex factor $\boldsymbol{\gamma}$ [10] as follows:

$$\tilde{\boldsymbol{y}} = \frac{\boldsymbol{y} - \boldsymbol{y}_{\text{empty}}}{\boldsymbol{\gamma}}. \tag{2.9}$$

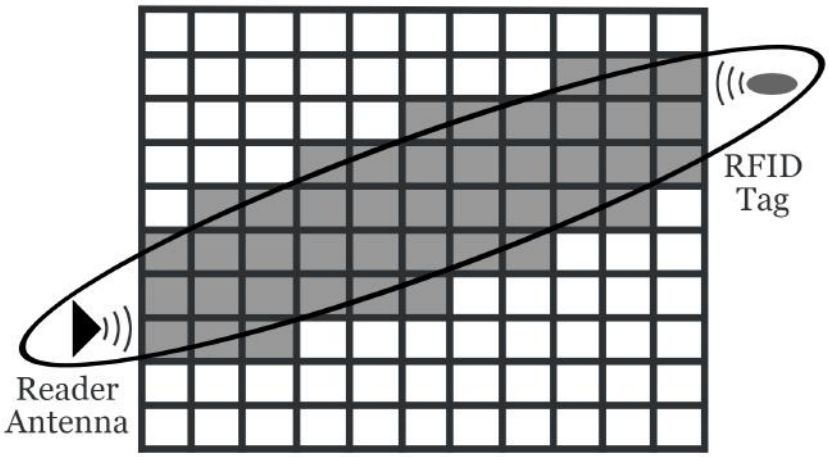

Figure 2.2: Ellipse Model

2.2.2 Modeling Reflections for Tomographic Imaging

The area of interest is divided in a grid of P cells. Each cell contributes to the resulting reflections by a factor x_p, noted as the (complex) *reflectivity*:

$$x_p = \left\{ \begin{array}{ll} 0, & \text{absence of a target} \\ a, & \text{presence of a target } \{a \in \mathbb{C} \mid a \neq 0\}, \end{array} \right\} \tag{2.10}$$

where $\mathbb{C}$ denotes the set of complex numbers.

Based on this, the components of the received signal can be modelled as:

$$y_k[m, f, n] = \sum_{p=0}^{P-1} x_p^{(k)} e^{-j\frac{2\pi}{\lambda_f}(d_k - d(m,n))}, \tag{2.11}$$

where $x_p^{(k)}$ are the cells' complex reflectivities, d_k is the distance of the propagation path of component k and $k = 0, 1, 2$, i.e., 0th, 1st and 2nd order reflections; in other words, there is a distinct complex reflectivity per cell for each reflection order k. The value $d(m, n)$ is subtracted because the one way line of sight was removed from the measurements by the complex factor $\boldsymbol{\gamma}$.

A coefficients matrix $\boldsymbol{A}^{(0)} \in \mathbb{C}^{MFN \times P}$ is constructed corresponding to the

0th order Reflections with the following elements:

$$A^{(0)}[i,p] = e^{-j\frac{2\pi}{\lambda_f}(2\cdot d(m,p)-d(m,n))}, \tag{2.12}$$

where $i = 0, 1, \ldots, MFN-1$, $m = \lfloor i/(FN) \rfloor$, $f = \lfloor i/N \rfloor \mod F$.

Similarly, two coefficients matrices $\boldsymbol{A}^{(1)} \in \mathbb{C}^{MFN\times P}$ and $\boldsymbol{A}^{(2)} \in \mathbb{C}^{MFN\times P}$ are constructed corresponding to the 1st and 2nd order reflections respectively, with the following elements:

$$A^{(1)}[i,p] = e^{-j\frac{2\pi}{\lambda_f}(d(m,n)+d(m,p)+d(p,n)-d(m,n))}, \tag{2.13}$$

$$A^{(2)}[i,p] = e^{-j\frac{2\pi}{\lambda_f}(2\,(d(m,n)+d(p,n))-d(m,n))}, \tag{2.14}$$

where $n = (i \mod N)$.

Finally, the ellipse model is implemented. An elliptical shape surrounding the antenna and tag represents the electromagnetic Fresnel ellipsoid, which is associated with diffraction patterns around an obstacle. It describes the area around the line-of-sight (LOS) of a link that can significantly influence it and provides a simpler process for identifying which cells are in the LOS path. Consequently, the elements of matrices $\boldsymbol{A}^{(k)}$ are set to 0 if $d(m,n) + d(m,p) - d(p,n) > \Lambda$, where Λ is a parameter that adjusts the width of the ellipse.

2.3 Compressive Sensing

Compressive sensing (or compressed sensing) is a technique in signal processing and statistics for efficiently reconstructing a signal by taking far fewer samples or measurements than traditionally required by the Nyquist-Shannon sampling theorem. This approach is particularly useful for signals that are sparse or compressible.

Specifically, compressive sensing tries to solve the following system:

$$\boldsymbol{y} = \boldsymbol{A}\boldsymbol{x} + \boldsymbol{n}, \tag{2.15}$$

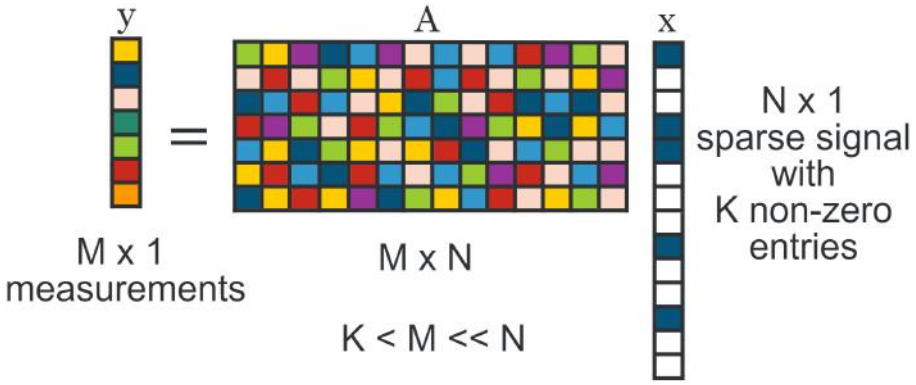

Figure 2.3: Compressive sensing system visualization.

where $\boldsymbol{y}$ is the vector of measurements, $\boldsymbol{A}$ is the measurement matrix, $\boldsymbol{x}$ is the original sparse signal and $\boldsymbol{n}$ represents noise. The goal is to recover $\boldsymbol{x}$ from $\boldsymbol{y}$ given that $\boldsymbol{x}$ is sparse.

To enforce sparsity to the solution, the number of nonzero components must be reduced. This can be achieved by solving an optimization problem that minimizes the l_0 norm of the solution vector. However, this is a challenging non-convex optimization problem (NP-hard). Therefore, it is commonly approximated by minimizing the l_1 norm, which is a convex relaxation and more tractable for efficient computation.

An important property that a measurement matrix must satisfy to guarantee sparse recovery is the Restricted Isometry Property (RIP). [26] [27]. A matrix $\boldsymbol{A} \in \mathbb{C}^{m \times d}$ is said to satisfy the RIP of order k if

$$(1-\delta)\|\boldsymbol{x}\|_2^2 \leq \|\boldsymbol{A}\boldsymbol{x}\|_2^2 \leq (1+\delta)\|\boldsymbol{x}\|_2^2 \tag{2.16}$$

for all $\boldsymbol{x} \in \sum_k$ with $\delta \geq 0$.

Although the RIP provides a foundation for deriving robust and stable results for general recovery algorithms, verifying it in practice is an NP-hard problem. A more practical (but more limited in terms of theoretical guarantees) alternative for evaluating a measurement matrix is the mutual coherence property.

Mutual coherence is the maximum correlation between any two columns of a matrix, and it should be minimized to ensure that the reconstruction

yields an accurate result. Considering a matrix $\boldsymbol{A} \in \mathbb{C}^{m \times d}$, the mutual coherence $\mu = \mu(\boldsymbol{A})$ is defined as:

$$\mu(\boldsymbol{A}) = \max_{1 \leq i \neq i \leq d} \frac{\langle \boldsymbol{a}_i, \boldsymbol{a}_j \rangle}{\|\boldsymbol{a}_i\|_2 \|\boldsymbol{a}_j\|_2}, \tag{2.17}$$

where $\boldsymbol{a}_i$ denotes the i-th column of $\boldsymbol{A}$.

2.4 Application of Compressive Sensing in DFL

In device-free localization, compressive sensing can be applied under the assumption that the human targets are not standing very close to each other. Based on the model described in Section 2.2.1, an l_1 minimization problem can be solved for each type of reflection. However, since all reflections share the same ground truth, each solution should have the same support, meaning they should have non-zero elements in the same positions. Therefore, instead of using the l_1 regularizer, the $l_{2,1}$ norm can be applied to enforce group sparsity.

In this method, a linear system is formed using the equations from all reflections. A composite matrix $\tilde{\boldsymbol{A}} \in \mathbb{C}^{MFN \times 3P}$ is composed of the matrices $\boldsymbol{A}^{(0)}$, $\boldsymbol{A}^{(1)}$, $\boldsymbol{A}^{(2)}$:

$$\tilde{\boldsymbol{A}} = \begin{bmatrix} \boldsymbol{A}^{(0)} & \boldsymbol{A}^{(1)} & \boldsymbol{A}^{(2)} \end{bmatrix} \tag{2.18}$$

and the solution vector $\tilde{\boldsymbol{x}} \in \mathbb{C}^{3P \times 1}$ is defined as:

$$\tilde{\boldsymbol{x}} = \begin{bmatrix} \boldsymbol{x}^{(0)\top} \boldsymbol{x}^{(1)\top} \boldsymbol{x}^{(2)\top} \end{bmatrix}^\top \tag{2.19}$$

Thus, offering the following system

$$\tilde{\boldsymbol{y}} = \tilde{\boldsymbol{A}} \tilde{\boldsymbol{x}} \tag{2.20}$$

The new optimization problem can be expressed as:

$$\hat{\tilde{\boldsymbol{x}}} = \arg\min_{\tilde{\boldsymbol{x}}} \frac{1}{2}\|\tilde{\boldsymbol{y}} - \tilde{\boldsymbol{A}}\tilde{\boldsymbol{x}}\|_2^2 + \tau\|\tilde{\boldsymbol{x}}\|_{2,1}, \tag{2.21}$$

where

$$\|\tilde{\boldsymbol{x}}\|_{2,1} = \sum_{p=0}^{P-1} \sqrt{\sum_{k=0}^{2} x_p^{(k)} \left(x_p^{(k)}\right)^*} \tag{2.22}$$

Then, the sub-vectors of $\hat{\tilde{\boldsymbol{x}}}$ are combined in a non-coherent way, using the l_2-norm which improves the signal-to-clutter ratio. Then the final vector is printed as an image which shows with hotter color the locations on which targets are most likely to exist.

To solve the above optimization problem, the "Sparse Reconstruction by Separable Approximation" (SpaRSA) toolbox is used. SpaRSA is an iterative algorithm designed for solving sparse signal recovery problems. In order to solve the problem efficiently, SpaRSA requires that the regularization parameter is chosen based on the following condition:

$$\tau = \zeta \left\| \tilde{\boldsymbol{A}}^{\dagger} \tilde{\boldsymbol{y}} \right\|_{\infty}, \quad \zeta = (0, 1), \tag{2.23}$$

For ζ larger than 1, the solution would be the zero vector. Values of ζ close to 1 promote group sparsity whereas values close to 0 relax this constraint.

Additionally, since the measurement matrix $\tilde{\boldsymbol{A}}$ is complex in this case, it is necessary to evaluate its block coherence instead of its mutual coherence. Block coherence captures the correlation between the different blocks of $\tilde{\boldsymbol{A}}$ and it takes values in the range $(0, 1)$. Block-coherence is defined as:

$$\begin{aligned} \mu_{\mathrm{B}}(\boldsymbol{A}) &= \max_{i,j \neq i} \frac{1}{d} \rho\left(\boldsymbol{A}^{(i)\dagger} \boldsymbol{A}^{(j)}\right), \\ \boldsymbol{A} &= \left[\underbrace{\tilde{\boldsymbol{a}}_1 \ldots \tilde{\boldsymbol{a}}_d}_{\boldsymbol{A}^{(0)}} \;\; \underbrace{\tilde{\boldsymbol{a}}_{d+1} \ldots \tilde{\boldsymbol{a}}_{2d}}_{\boldsymbol{A}^{(1)}} \;\; \underbrace{\tilde{\boldsymbol{a}}_{2d+1} \ldots \tilde{\boldsymbol{a}}_{3d}}_{\boldsymbol{A}^{(2)}} \right], \end{aligned} \tag{2.24}$$

where $\boldsymbol{A}^{(i)}, i \in \{0, 1, 2\}$ are l_2-normalized sub-matrices of $\tilde{\boldsymbol{A}}$ and d is equal to the size of each block (number of cells). As in the case of mutual coherence, block coherence should be as low as possible.

The SpaRSA algorithm can be initialized in four ways: zero initialization, random initialization, initialization with $\tilde{\boldsymbol{A}}\tilde{\boldsymbol{y}}$ or a custom initialization provided by the user. After testing each method, it was observed that the final solution of the system remained unchanged. Consequently, random initialization was chosen.

The SpaRSA algorithm is not inherently monotone, meaning the objective function is not guaranteed to decrease at every iteration. However, by tuning the internal parameter α_t appropriately, a decrease in the objective function at each step can be ensured. The option for monotonic decrease is available in the SpaRSA configuration and is therefore enabled.

Moreover, when the signal is not very sparse, SpaRSA tends to be considerably slower in both identifying the correct support for $\tilde{\boldsymbol{x}}$ and achieving convergence in its final stages. To tackle this problem, a continuation strategy is employed. Initially, the system is solved for a larger τ than the target value. Then, τ is gradually decreased to the specified value, with each iteration using the previous solution as a warm start. This approach significantly reduces the overall computation time compared to solving the problem for the given τ from a cold start.

Lastly, the following convergence criterion was chosen:

$$\frac{\|\tilde{\boldsymbol{x}}^{(t)} - \tilde{\boldsymbol{x}}^{(t-1)}\|_2}{\|\tilde{\boldsymbol{x}}^{(t)}\|_2} \leq \epsilon, \tag{2.25}$$

where $\epsilon \in (10^{-2}, 10^{-8})$ corresponds to the tolerance parameter.

SpaRSA includes an optional post-processing step, called debiasing, aimed at eliminating the attenuation of signal magnitude due to the presence of the regularization term. In this step, the algorithm sets the zero groups in the solution vector to zero and then solves the following problem with the remaining non-zero elements:

$$\min_{\tilde{\boldsymbol{x}}} \frac{1}{2}\|\tilde{\boldsymbol{A}}_{\boldsymbol{I}}\tilde{\boldsymbol{x}}_{\boldsymbol{I}} - \tilde{\boldsymbol{y}}\|_2^2 \tag{2.26}$$

where $\boldsymbol{I}$ is the set of indices of the nonzero components of the initial SpaRSA solution, $\tilde{\boldsymbol{A}}_{\boldsymbol{I}}$ is the column submatrix of $\tilde{\boldsymbol{A}}$ corresponding to $\boldsymbol{I}$, $\tilde{\boldsymbol{x}}_{\boldsymbol{I}}$ and is the

subvector of unknowns for $\boldsymbol{I}$. This final step improves the balance of weights among different targets, preventing some targets from having large weights while others barely appear in the heatmap.

Chapter 3

Phase Method with Read Rate

3.1 Introduction

Prior art [18] has examined the effects of human presence and movement on the phase and read rate measurements of RFID links. It has been demonstrated that when a human target crosses the line-of-sight (LOS) of an RFID link, the phase measurements show significant fluctuations. Furthermore, the number of reads from the link's RFID tag decreases or may cease altogether. By exploiting these observations and the human geometry, the movement of single target was tracked with high accuracy. However, the proposed method has significant limitations due to the need for prior offline computation and knowing the number of targets in advance. Thus, a new method is examined which combines the phase and read rate fluctuations with Radio Tomographic Imaging [4] to localize multiple targets without the need of prior knowledge.

3.2 Version 1

The method consists of two phases. In the offline phase, read rate (ρ_{empty}) and phase (ϕ_{empty}) measurements are taken from each link when the area of interest is free of targets. Then, in the online phase, as human targets inhabit the area, new measurements of read rate ($\rho_{occupied}$) and phase ($\phi_{occupied}$) are obtained and the following quantities are calculated for each link:

$$\Delta\phi = \phi_{\text{occupied}} - \phi_{\text{empty}}, \tag{3.1}$$

$$\Delta\rho = \frac{\rho_{\text{occupied}}}{\rho_{\text{empty}}}. \tag{3.2}$$

To differentiate between the links that are affected by the target and those that are not, thresholds can be set for each quantity. When either the phase or read rate change exceeds its specified threshold, denoted as γ_ϕ and γ_ρ respectively, the corresponding link is considered affected or "shadowed".

The area of interest is divided in a grid of P cells. Then each cell is assigned a weight based on the shadowed links that pass over it. Specifically, the weight of cell p is assigned the following weight:

$$x_p = \sum_{l=1}^{L} \frac{1}{\sqrt{d(m_l, n_l)}} \delta_l^p, \ p = 1, 2, \ldots, P, \tag{3.3}$$

$$\delta_l^p = \begin{cases} 1, & \text{if } d(m_l, n_l) + d(m_l, p) - d(p, n_l) < \Lambda \text{ and} \\ & (\Delta\phi_l > \gamma_\phi \text{ or } \Delta\rho_l > \gamma_\rho) \text{ and} \\ & d(m_l, p) > u \\ 0, & \text{otherwise} \end{cases}, \tag{3.4}$$

where $d(m_l, n_l)$ is the distance between reader antenna m_l and tag n_l, $d(m_l, p)$ is the distance between reader antenna m_l and cell p and $d(p, n_l)$ is the distance of between tag n_l and cell p corresponding to link l.

The parameter u is the antenna-cell distance threshold used to ensure that cells close to the antennas are not assigned weights. This threshold is applied because many links pass through these cells, leading them to have large weights irrespective of whether a target is present in their location and thus producing false results.

The factor $\frac{1}{\sqrt{d(m_l, n_l)}}$ is used to lower the impact of long-distance links. These links are more prone to noise due to the increased distance between the antenna and the tag, and therefore should not be heavily relied upon.

The above weights constitute the solution vector $\boldsymbol{x} \in \mathbb{R}^{P \times 1}$ and are printed as an image which shows with hotter color the locations on which targets are most likely to exist.

3.3 Version 2

The method described above has the challenge of relying on threshold choices, which may not always reflect real-life conditions accurately. To complement this, an alternative weight is introduced that rates the shadowing instead of just marking a link as shadowed or not.

After the quantities $\Delta\phi$ and $\Delta\rho$ are calculated for each link, they are normalized and combined to produce the following weight:

$$w_l = \frac{\tilde{\Delta\phi}_l}{\tilde{\Delta\rho}_l},\ l = 0, 1, \ldots, L, \tag{3.5}$$

where $\tilde{\Delta\phi}_l$ is the normalized phase difference and $\tilde{\Delta\rho}_l$ is the normalized read rate difference of link l. If a link is not read when the room is occupied, $\rho_{\text{occupied}} = 0 \Rightarrow \Delta\rho_l = \tilde{\Delta\rho}_l = 0$ and thus the weight w_l becomes infinite. In this case, the weight is assigned the maximum value of the other finite weights.

Then, each cell p of the area's grid is assigned the following weight:

$$x_p = \sum_{l=1}^{L} \frac{1}{\sqrt{d(m_l, n_l)}} \delta_l^p w_l,\ p = 1, 2, \ldots, P, \tag{3.6}$$

$$\delta_l^p = \begin{cases} 1, & \text{if } d(m_l, n_l) + d(m_l, p) - d(p, n_l) < \Lambda \text{ and} \\ & d(m_l, p) > u \\ 0, & \text{otherwise} \end{cases}, \tag{3.7}$$

where u is the antenna-cell distance threshold.

The above weights constitute the solution vector $\boldsymbol{x} \in \mathbb{R}^{P\times 1}$ and are printed as an image which shows with hotter color the locations on which targets are most likely to exist.

Chapter 4

Fusion Scheme for different DFL Methods

4.1 Introduction

To take full advantage of the information acquired by the signal measurements and utilize the potential of various techniques, a fusion scheme is examined. Multiple device free localization techniques based on tomographic imaging can be combined in order to enhance the localization. Although each technique may based on different signal characteristics, they all generate a heatmap depicting potential target locations within the area of interest. Therefore, combining these techniques becomes possible, improving overall accuracy.

4.2 Fusion Scheme

After the solution vector of each method is produced and the respective cell weights are obtained, a particle for each cell is generated and placed on the grid. The weight of each particle is the product of the normalized weights of each method's cell weight corresponding to that particle:

$$w_p = w_p^{(i)} \times w_p^{(j)},\ p = 0, 1, \ldots, P, \tag{4.1}$$

where w_p is the combined weight, $w_p^{(i)}$ is the weight from method i and $w_p^{(j)}$ is the weight of method j, for cell p.

In this approach, regions where both methods indicate a high likelihood of a target's presence, increase confidence through mutual reinforcement.

On the other hand, areas where discrepancies arise regarding the target's presence cancel out each other. Then, the particles with the new weights can be grouped with a clustering method and used the targets' location estimation.

4.3 Noise Reduction Techniques

From the resulting images of the presented methods, as well as results from prior art, it can be observed that there is a significant amount of noise that can decrease the localization accuracy. Thus, two noise reduction techniques are utilized.

The following weight scaling technique can be applied to reduce the noise in the solution:

$$\tilde{w}_p = \frac{w_p^s}{\sum_p w_p^s}, \tag{4.2}$$

where s is the scaling power. By raising the weights to higher powers, their differences are amplified: large weights are emphasized, while small weights diminish. This results in a clearer image.

To further reduce noise and enhance the performance of clustering algorithms in multi-target scenarios, weights smaller than the mean are removed. This approach facilitates better separation and easier recognition of targets.

However, these noise reduction techniques can have drawbacks. If the localization method is suboptimal, weight scaling and removal may increase confidence in potentially inaccurate results, ultimately leading to poorer accuracy.

Chapter 5

Experiments

5.1 Introduction

To test and compare the presented methods with prior art, real world experiment were conducted. The RFID reader that was used was the Impinj R420, equipped with 4 antenna ports, operating within the frequency range of $865-868$ MHz and a maximum power output of 31.5 dBm. The experiments were conducted in a large area measuring 4 m $\times$ 4 m. The antennas MT-242017/NRH/K from MTI Wireless Edge were employed, featuring RHCP polarization and a gain of $10-11$ dBic. RSSI, phase and read rate measurements were collected at intervals of 0.5 seconds during the experiments. To maximize tag read rates, the reader was configured to operate in *Max Throughput* mode.

A total of 84 UHF EPC Gen 2 RFID tags were utilized, evenly distributed along all sides, with one antenna positioned on each side, as illustrated in Figure 5.1 (left). The primary objective of this layout was to maximize the number of crossing links, ensuring their uniform distribution throughout the area. A visualization of the number of links that cross each cells in the area is given in Figure 5.1 (right).

During the experiments, the following methods were tested: Radio Tomographic Imaging [4] (referred to as the RSSI Method), Phase Method with RF Propagation presented in Chapter 2 (referred to as Phase Method I), Phase Disturbances Method [18] (referred to as Phase Method II), and both versions of Phase Method with Read Rate presented in Chapter 3 (referred to as Phase Method III (Ver.1) and (Ver.2)). Additionally, various combinations of these methods using the fusion technique were examined and the best of them is presented.

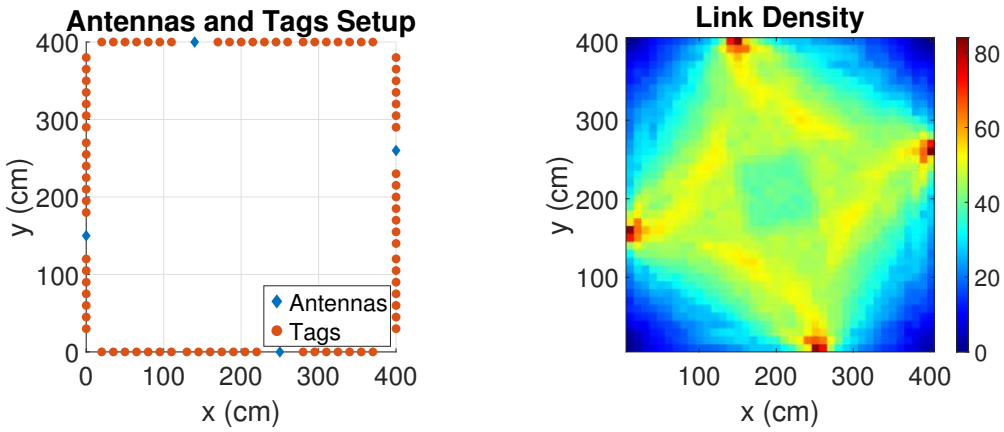

Figure 5.1: Setup of reader antennas and RFID tags and Link Density.

5.2 Phase Disturbances Method Modification

The Phase Disturbances Method proposed in [18], is applied in a tracking scenario, where one target moves in the area of interest and phase and read rate measurements, as well as particle filtering is used to track their movement. To adapt this method in a static scenario, where the measurements of a time instant do not depend on the past, and in a multiple targets scenario, a few changes have been made. The modified method is presented below.

During the offline phase, a matrix is constructed based on the geometric characteristics of the target, utilizing a setup with N tags and M antennas. The human target is modeled as a circle with radius R. Due to its volume, when they cross the line of sight of a RFID link, they cause shadowing and affect the phase and read rate measurements. In order to keep track of which links are shadowed in each target location, matrix $\boldsymbol{E}(\boldsymbol{p}) \in \mathbb{R}^{N \times M}$ is constructed as follows:

$$E_{ij}(\boldsymbol{p}) = \begin{cases} 1, & \text{if } d(l_{ij}, \boldsymbol{p}) \leq R \\ 0, & otherwise \end{cases} \tag{5.1}$$

where $d(l_{ij}, p)$ is the perpendicular distance between the link's line-of-sight

line corresponding to tag i and antenna j and the center of the target and $\boldsymbol{p}$ is the location of the target. In the case of multiple targets, a matrix $\boldsymbol{E}(\boldsymbol{p}_1, \boldsymbol{p}_2, \ldots, \boldsymbol{p}_K) \in \mathbb{R}^{N \times M}$ is constructed for each combination of possible targets locations.

During the online phase, phase and read rate measurements are taken, in short time windows, with the target inside the area. Then a new matrix $\boldsymbol{M}^t \in \mathbb{R}^{N \times M}$ is constructed as follows:

$$M_{ij}^t = \begin{cases} 1, & \text{if } \Delta\phi^t > \gamma_\phi \text{ or } \Delta\rho^t > \gamma_\rho \\ 0, & otherwise \end{cases}, \tag{5.2}$$

where $\Delta\phi^t$ is the difference between phase measurements at time t and phase measurements of the empty area, $\Delta\rho^t$ is the difference between read rate measurements at time t and read rate measurements of the empty area and γ_ϕ and γ_ρ are the phase and read rate thresholds, respectively.

Finally, a weight is assigned to each cell p based on the (dis)similarity between the matrix $\boldsymbol{M}^t$ and $\boldsymbol{E}(p)$:

$$x_p = \frac{\sum_{j=1}^{M} \sum_{j=i}^{N} M_{ij}^t E_{ij}(p)}{\sum_{j=1}^{M} \sum_{j=i}^{N} |M_{ij}^t - E_{ij}(p)|} \tag{5.3}$$

5.3 Phase Method I - Regularization Parameter

The SpaRSA toolbox requires that the regularization parameter is chosen as follows:

$$\tau = \zeta \left\| \tilde{\boldsymbol{A}}^\dagger \tilde{\boldsymbol{y}} \right\|_\infty, \quad \zeta = (0, 1), \tag{5.4}$$

where ζ controls the effect of the regularizer.

Several tests were conducted with scenarios involving 1, 2, and 3 targets to identify the most suitable value of ζ. The results are illustrated in Figure 5.2. For a single target, the mean absolute error decreases as the value of ζ increases, reaching its minimum in the range of $[0.7, 0.8]$, before rising again. Conversely, in the multiple target scenarios, localization accuracy diminishes

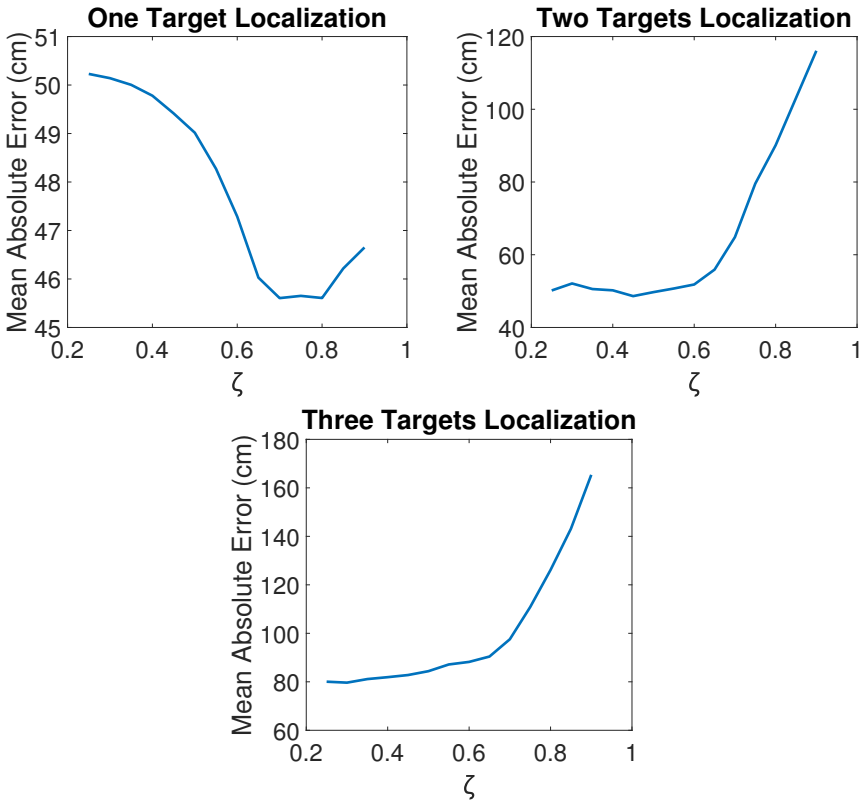

Figure 5.2: Phase Method I - Regularization Parameter

as ζ increases. Therefore, to effectively localize multiple targets, ζ should be set close to 0.25.

5.4 Localization Images

After obtaining the solutions from each method, the solution vectors are reshaped into matrices representing the cell grid. These matrices are then displayed as heatmap-like images, where the color of each pixel corresponds to its respective cell's weight. Example images for localizing 1, 2, and 3 targets using the different methods are shown in Figures 5.3 to 5.5, respectively. More examples of all the positions tested are given in Appendix A.

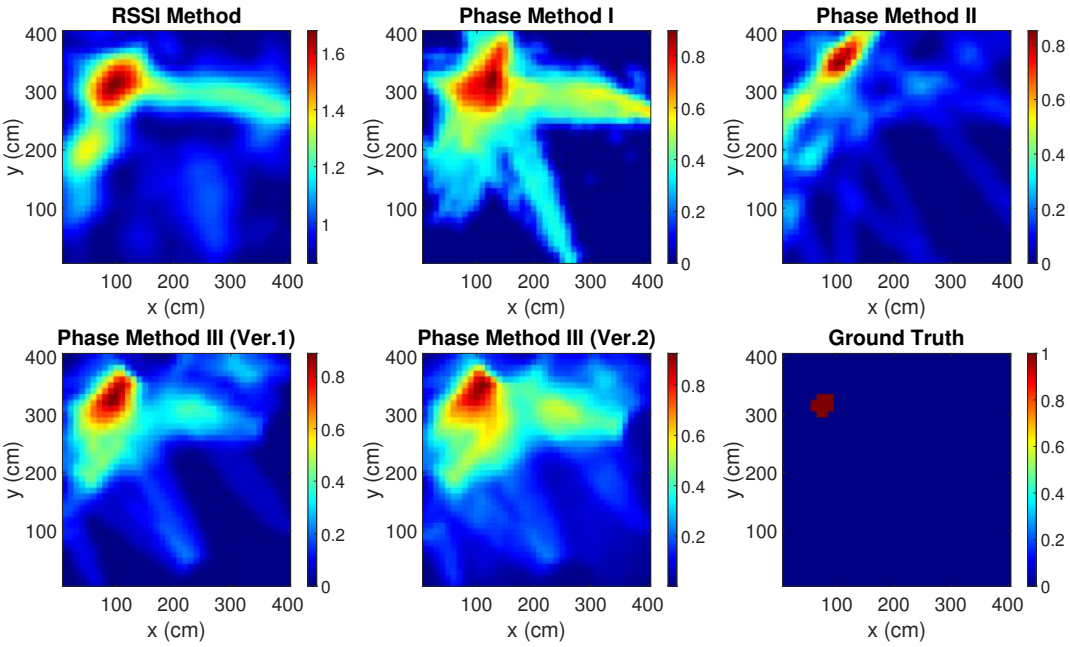

Figure 5.3: One Target Localization

5.4.1 One Target Localization

In Figure 5.3, it can be seen that all methods successfully localize the target with high accuracy. Among the methods, Phase Method I and Phase Method III (Ver.2) produce the noisiest images, whereas Phase Method II achieves the highest level of accuracy.

5.4.2 Two Targets Localization

In the case of two targets (Figure 5.4), all methods successfully localize both targets with good accuracy and equal intensity.The RSSI Method has the least amount of noise and, along with both versions of Phase Method III, provides the clearest images. Phase Method I results in less uniform target shapes, with one target appearing more pronounced than the other. Phase Method II has generated some artifacts with high weights, which can decrease the localization accuracy.

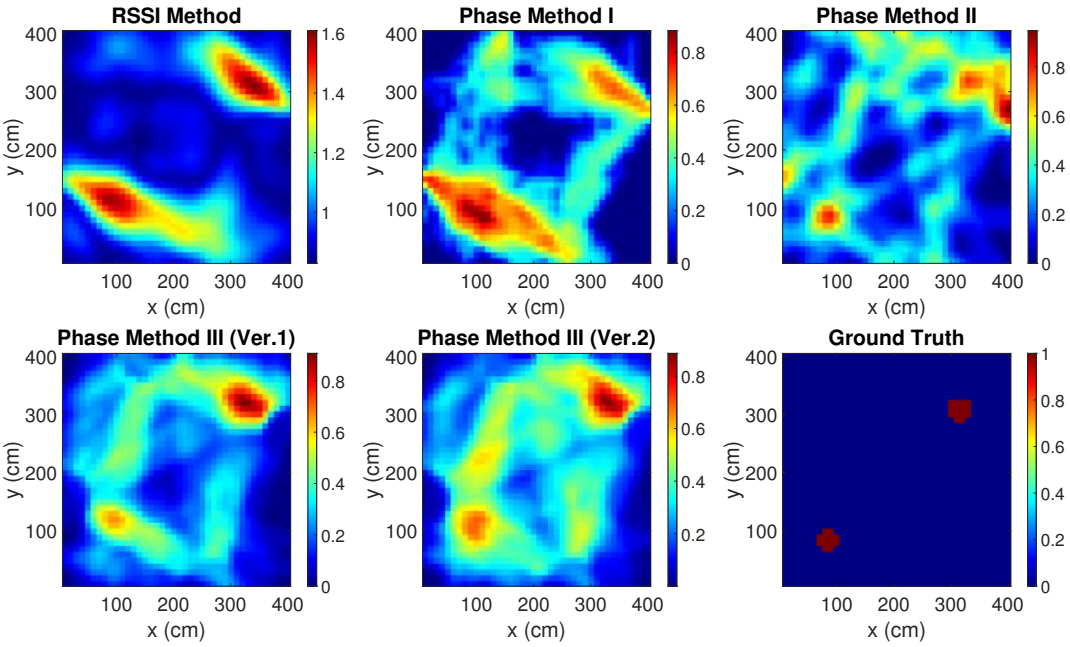

Figure 5.4: Two Targets Localization

5.4.3 Three Targets Localization

Good localization accuracy can also be achieved in the three targets scenario, provided that the targets are not standing very close to each other. Figure 5.5 shows the corresponding images for different methods. In this scenario, both versions of Phase Method III achieve good results, as the targets have similar intensity, are clearly defined, and are close to their true location. On the other hand, Phase Method I and the RSSI Method have not localized the bottom left target accurately and the former is less precise. In addition, Phase Method II has good accuracy, but one of the targets is emphasized, while the others are very vague and not well defined.

5.4.4 Fusion of different methods

In Figure 5.6 three localization scenarios are presented in order to compare the fusion of the RSSI method with Phase Method III (Ver.1) with each method individually. The results clearly show that the combination significantly enhances the accuracy of the images.

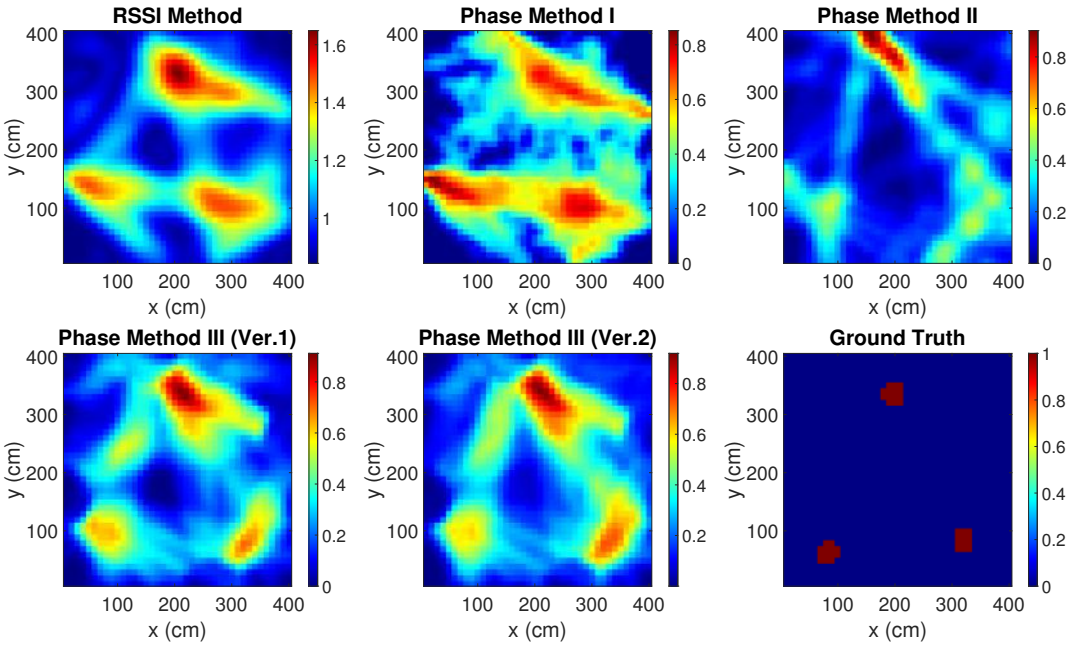

Figure 5.5: Three Targets Localization

The combined method shows less noise than the RSSI method in the one target scenario (first row), with the noise being less pronounced, making the targets more distinguishable. In the scenarios of two and three targets localization (second and fourth rows), the images produced by the combined method show more clearly defined target shapes than those generated by either the RSSI method or Phase Method III alone. Additionally, the combination method mitigates the high-weight artifacts in Phase Method III images which become less noticeable in the combined method images.

In the third and fifth rows, the combined method effectively differentiates between targets standing as close as 1.3 meters apart. The RSSI method fails to distinguish between targets in the two-target scenario and cannot localize the lower target in the three-target scenario. On the other hand, Phase Method III performs well in the two-target scenario, but cannot separate the two upper targets in the three-target scenario. However, when the two methods are fused, the results show clearly defined targets with high localization accuracy.

Overall, the combined method's images more closely match the ground

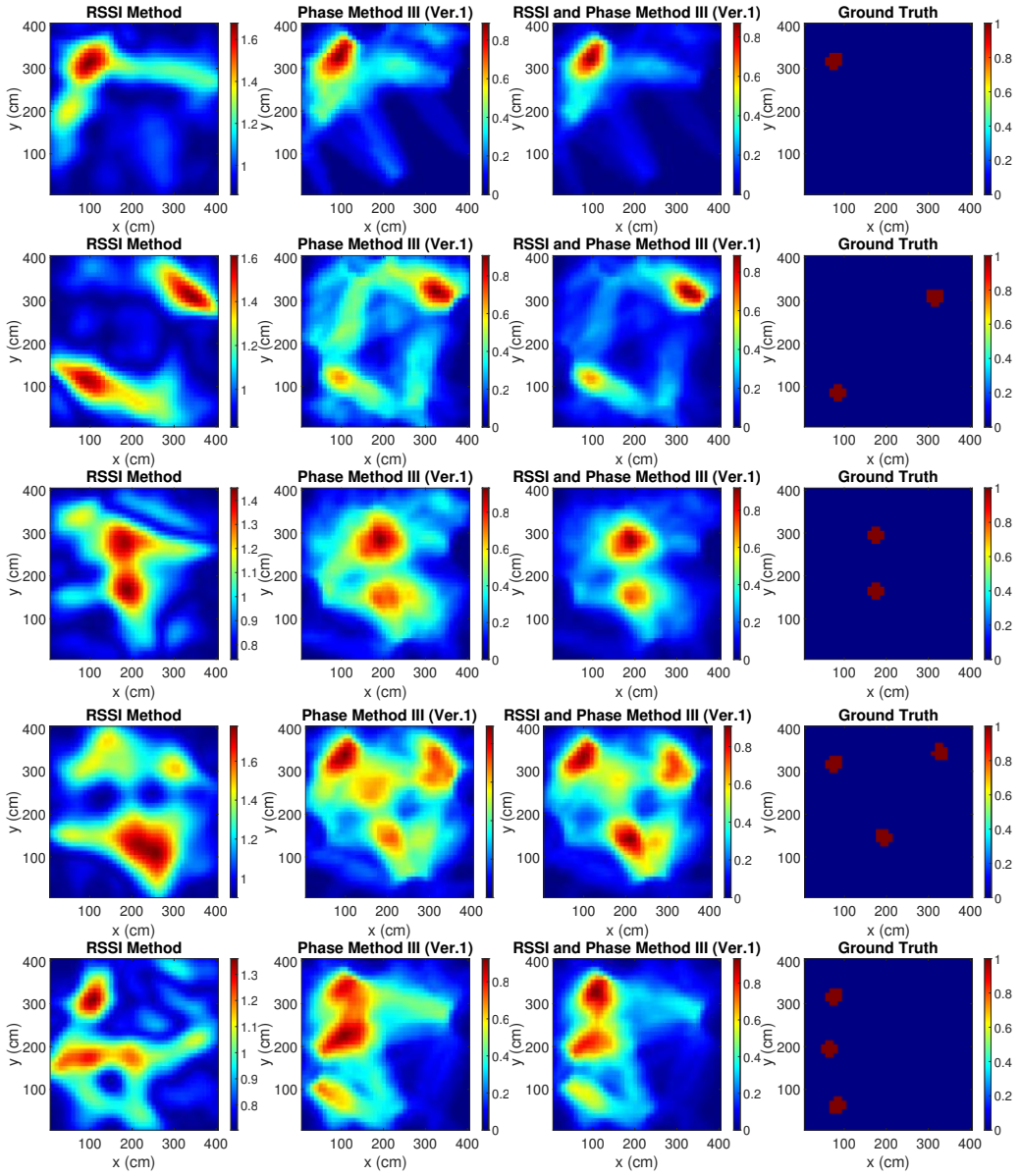

Figure 5.6: Fusion of RSSI Method and Phase Method III (Ver.1)

truth in terms of target placement and shape, offering a substantial improvement in image quality by reducing noise, enhancing target definition, and minimizing artifacts.

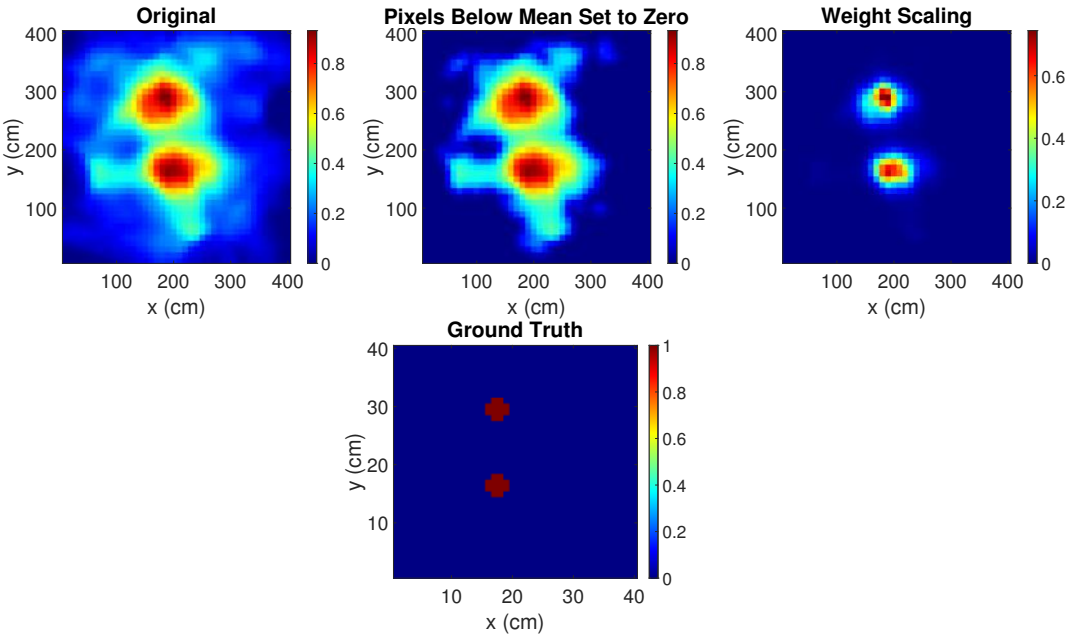

Figure 5.7: Noise Reduction Techniques

5.5 Noise Reduction

To reduce the noise in the produced images, two techniques are applied. First, the mean value of the cell weights is calculated, and cells with weights smaller than the mean are set to zero. This thresholding technique effectively eliminates low-intensity noise, thereby enhancing the contrast of the significant features in the image. Next, weight scaling is performed to emphasize large weights and dampen smaller ones. This step amplifies the cells corresponding to the actual targets while further suppressing the residual noise. These techniques result in more precise and better-separated target locations, as shown in Figure 5.7.

5.6 Weights' Scaling Comparison

To reduce noise effects and improve localization accuracy, a weight scaling technique is applied. This technique amplifies the differences between weights, thereby emphasizing the higher values. However, if the localization

method's performance is suboptimal, aggressive scaling can worsen the results. To find the best scaling factor, a range of scaling powers from 1 to 20 is tested. Figure 5.8 shows the mean absolute error of Phase Method III for different scaling powers in the 1, 2, and 3 targets localization scenarios.

Figure 5.8: Weight Scaling Comparison using Phase Method III

From Figure 5.8, it is evident that in all scenarios, increasing the scaling power reduces localization error up to a certain point, beyond which the error starts to increase again. The optimal scaling power, where the lowest localization error is achieved, varies across different scenarios. For localizing a single target, the optimal scaling power is 9, whereas for localizing two and three targets, the optimal values are 7 and 5, respectively. The decrease in the optimal value can be explained by the fact that as the number of targets increases, the method's performance decreases. Consequently, higher scaling powers that enhance confidence in the results can actually reduce accuracy in multi-target scenarios.

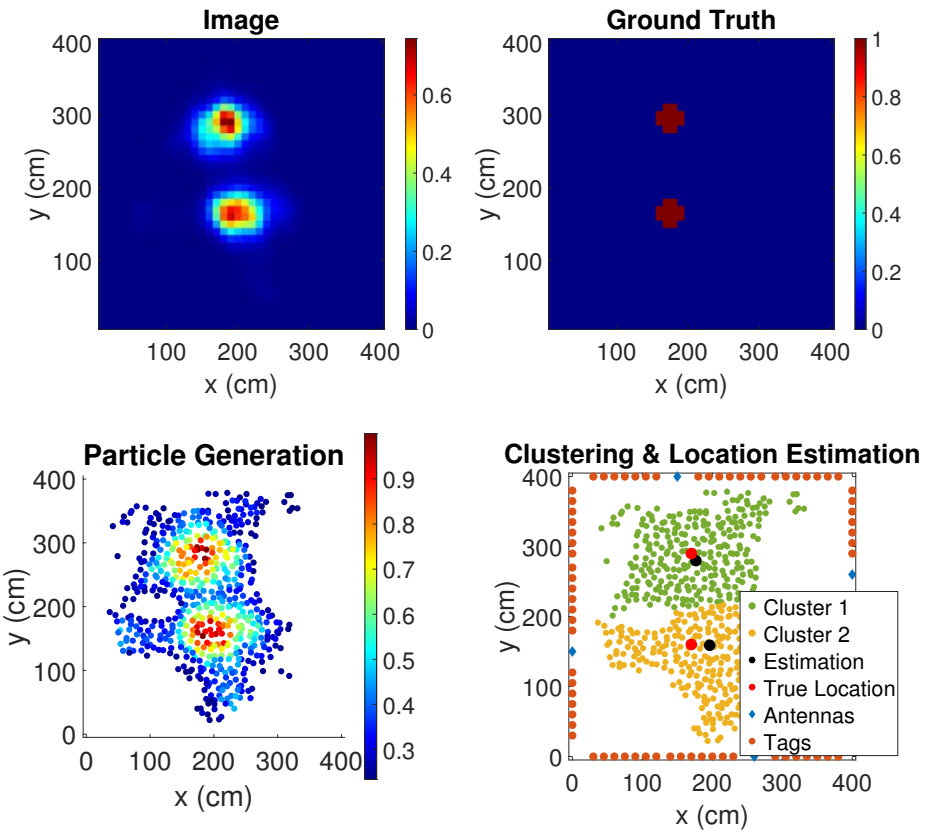

Figure 5.9: Clustering and Location Estimation

5.7 Clustering

The solutions produced by the examined methods are cell weights, which, when visualized, generate a heatmap of the area. This heatmap can display the general locations of the targets. However, to get their exact coordinates, clustering techniques are required. In this study, two clustering methods are tested: k-Means and Expectation Maximization (with or without constant variance). The clustering and location estimation process is illustrated in Figure 5.9. Starting with the original image (upper left), a particle is randomly generated within each cell's area, as shown in the lower left image. These particles are then clustered, and the weighted sum of the particles within each cluster represents the estimated location of the target, depicted in the lower right image.

Table 5.1: Comparison of Clustering Methods

	Two Targets			Three Targets		
Method \Clustering (cm)		K-Means	Expectation Maximization		K-Means	Expectation Maximization
RSSI Method	Error1	23,5891	**23,6887**	Error1	36,8433	34,4633
	Error2	**40,9609**	**39,3025**	Error2	56,7304	67,8255
				Error3	142,6888	166,1056
Phase Method I	Error1	42,9828	49,8643	Error1	46,4592	46,0359
	Error2	73,5556	77,7159	Error2	68,3405	77,7037
				Error3	144,7515	168,7185
Phase Method II	Error1	**19,6641**	33,3187	Error1	32,0858	37,6674
	Error2	63,971	90,4208	Error2	53,9672	**65,9395**
				Error3	152,1529	145,3417
Phase Method III (Ver.1)	Error1	21,0942	24,9431	Error1	**24,6085**	**29,4873**
	Error2	47,4255	60,431	Error2	**44,9929**	57,7267
				Error3	**106,6253**	135,8147
Phase Method III (Ver.2)	Error1	24,4129	29,9857	Error1	30,8088	35,6984
	Error2	53,3341	64,5713	Error2	49,5435	67,1456
				Error3	114,1934	**130,2004**

5.7.1 k-Means Clustering

k-Means clustering is a popular unsupervised machine learning algorithm used for grouping set of particles into a pre-defined number of clusters, k. Each cluster is defined by its centroid, which is the mean position of all the points in that cluster. The algorithm is iterative and in each step, it assigns each data point to the nearest centroid and then updates the centroids based on the mean of the points assigned to them. This process repeats until a convergence or a maximum iteration criterion is satisfied.

5.7.2 Expectation Maximization

Expectation Maximization (EM) is a clustering method that can model clusters with different shapes and sizes by fitting a mixture of Gaussian distributions to the data. The algorithm consists of two steps: the Expectation step (E-step) and the Maximization step (M-step). In the E-step, the algorithm calculates the probability of each data point belonging to each cluster based on the current estimates of the cluster parameters. In the M-step, it updates the cluster parameters (mean, variance, and mixing coefficients) to maximize the likelihood of the data given these probabilities. EM can work with data of varying cluster densities and shapes. However, given that humans are modeled as circles with a constant radius, a variant of the EM algorithm with a constant diagonal covariance matrix is also tested.

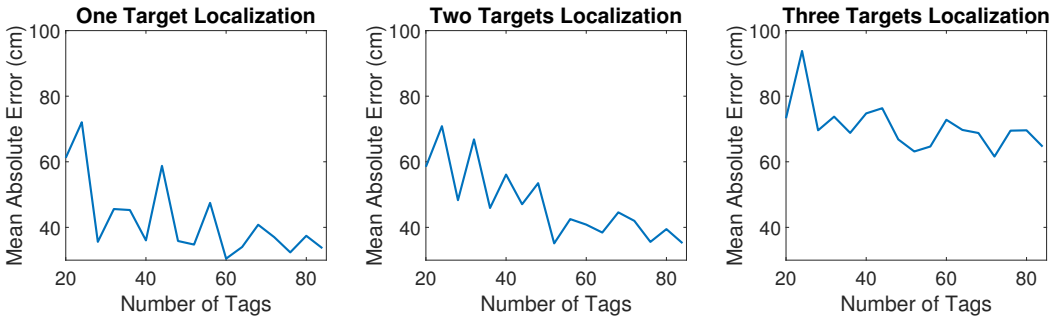

Figure 5.10: Impact of the number of deployed tags.

The comparison between the two clustering methods is illustrated in Table 5.1. The results indicate that k-Means consistently produces better outcomes than Expectation Maximization (EM). Both algorithms were run with the assumption that the number of targets was known a priori. The superior performance of k-Means can be attributed to its use of the ℓ_2-norm for clustering the data, which biases it towards spherical clusters. Given that the system models targets as circular volumes, k-Means is better suited for this task. The results demonstrate that k-Means yields lower errors in both two-target and three-target scenarios, highlighting its effectiveness in accurately clustering the data in the given context.

5.8 Number of Tags

The RFID tags deployed in the area act as additional antennas, providing spatial diversity. Therefore, it is important to examine how the number of tags affects localization accuracy. Utilizing the Phase Method III (Version 1), multiple experiments were conducted, each using measurements from a different number of tags. The results for scenarios with 1, 2, and 3 targets are displayed in Figure 5.10.

The results indicate that increasing the number of tags reduces localization error. Despite some fluctuations, overall performance improves across all tested scenarios. Consequently, the number of tags significantly enhances localization accuracy. Given the cost-effectiveness of the tags, it is feasible to deploy hundreds or even thousands of tags to achieve optimal results.

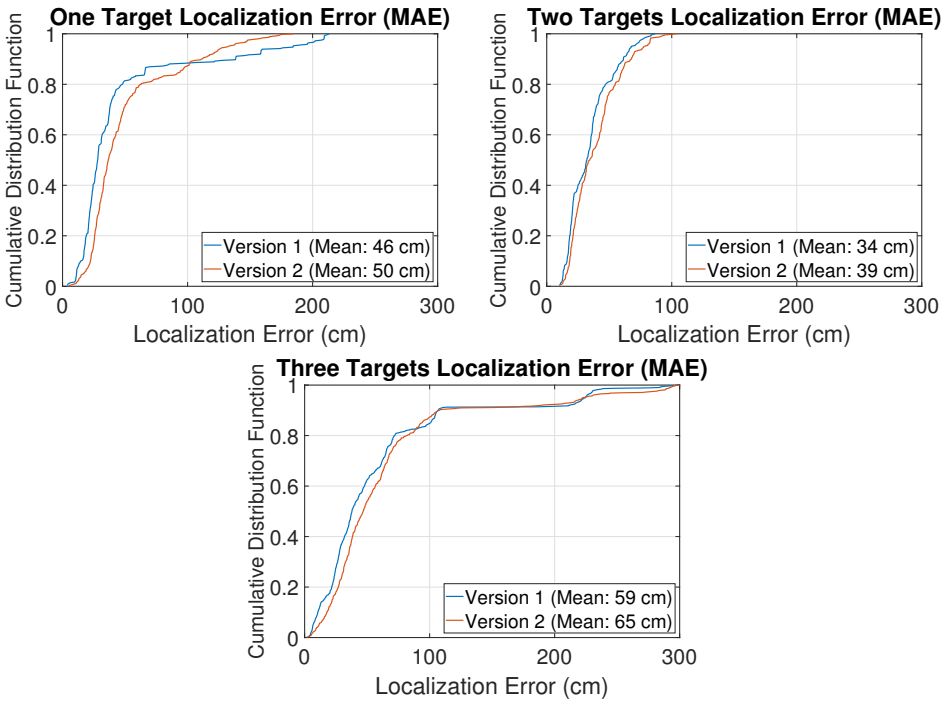

Figure 5.11: Phase Method III - Ver. 1 vs Ver.2 CDFs

5.9 Phase Method with Read Rate - Ver. 1 vs Ver.2

The comparison between Version 1 and Version 2 for localization errors is depicted through three cumulative distribution function (CDF) plots in Figure 5.11, each representing scenarios with one, two, and three targets.

In the one target localization scenario, Version 1 demonstrates superior performance with a mean error of 46 cm, while Version 2 has a slightly higher mean error of 50 cm. The CDF curve for Version 1 reaches higher cumulative distribution values at lower localization errors, indicating more accurate localization compared to Version 2.

In the two targets localization scenario, Version 1 again outperforms Version 2. Version 1 achieves a mean error of 34 cm, whereas Version 2 has a mean error of 39 cm. The CDF curve for Version 1 is positioned to the left of that for Version 2, displaying lower localization errors at comparable

cumulative distribution values.

Similar results are shown in the three targets localization scenario. Version 1 has a mean error of 59 cm, compared to Version 2's mean error of 65 cm. The CDF curve for Version 1 is slightly better, indicating that Version 1 maintains more accurate localization even with an increased number of targets.

Overall, across all three scenarios, Version 1 consistently exhibits better performance with lower mean localization errors compared to Version 2.

5.10 Cumulative Distribution Functions

For the localization of 1 to 3 targets, 30 independent windows of measurements were taken for various targets positions. From these measurements, estimates of the target locations were calculated as well as the mean absolute error (MAE) and cumulative distribution functions (CDF) of localization error. Specifically, when multiple human targets were present, errors for each localization experiment were sorted, with Error 1 being the smallest and Error 2 (or Error 3) the largest for the scenarios involving two (or three) targets. The results are illustrated in Figures 5.12 to 5.14.

In the implementation of the different tomographic methods, the following parameter values were used: the width of the ellipse model for the RSSI, Phase Method I and Phase Method III (both versions) was set to $\Lambda = 5$ cm; the SpaRSA regularization parameter in Phase Method I was set to $\zeta = 0.25$; for the RSSI Method, the covariance matrix C_x was used for regularization, with $\delta_c = 10$ cm ("space constant" correlation parameter) and $\sigma_x^2 = 0.001$ (variance at each cell); for Phase Method II and Phase Method III (Version 1), the phase difference and read rate thresholds were set to $\gamma_\phi = 1$ rad and $\gamma_\rho = 0.25$ respectively and the human radius was set at 20 cm. This parameters were also used in Table 5.1 and Figures 5.3 to 5.6.

Figure 5.12 indicates that most methods can accurately localize a single target, achieving an 80th percentile error of just 60 cm. The RSSI Method, Phase Method III, and Phase Method II have similar performance, although Phase Method II slightly outperforms the others in terms of lower errors.

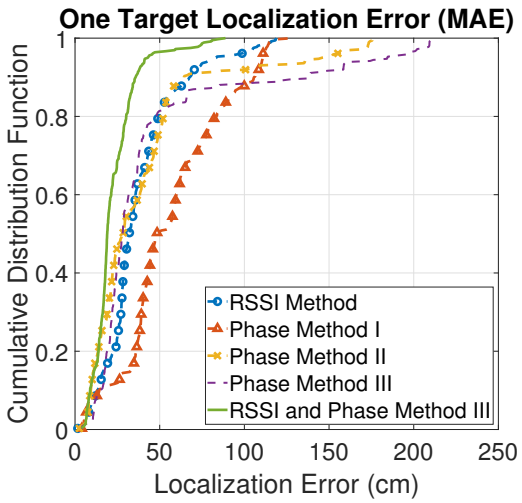

Figure 5.12: CDF of the localization error of 1 target using the 5th power for scaling.

Notably, combining the RSSI Method with Phase Method III surpasses the individual methods, achieving a mean absolute error of 22.6 cm using the fusion method presented in this work. Phase Method I lags behind, producing comparable results only 60% of the time.

In the case of two human targets shown in Figure 5.13, all localization methods can accurately locate the first target, but the accuracy for the second target diminishes. The RSSI Method and Phase Method III maintain good performance for both targets, whereas Phase Methods II shows a significant drop in performance for the second target. The combination of the RSSI Method with Phase Method III improves the localization of the first target and yields the best error for the second target. Phase Method I produces the largest errors for both targets.

A similar trend is observed in Figure 5.14 for three targets. The positional error for the first two targets remains acceptable across most methods. The combination of the RSSI Method and Phase Method III, using the fusion method of this work, delivers superior performance with lower error rates. However, all methods struggle with localizing the third target, resulting in a mean absolute error exceeding 1 m. The poor localization of the third target is likely due to target interaction affecting RF propagation, highlighting

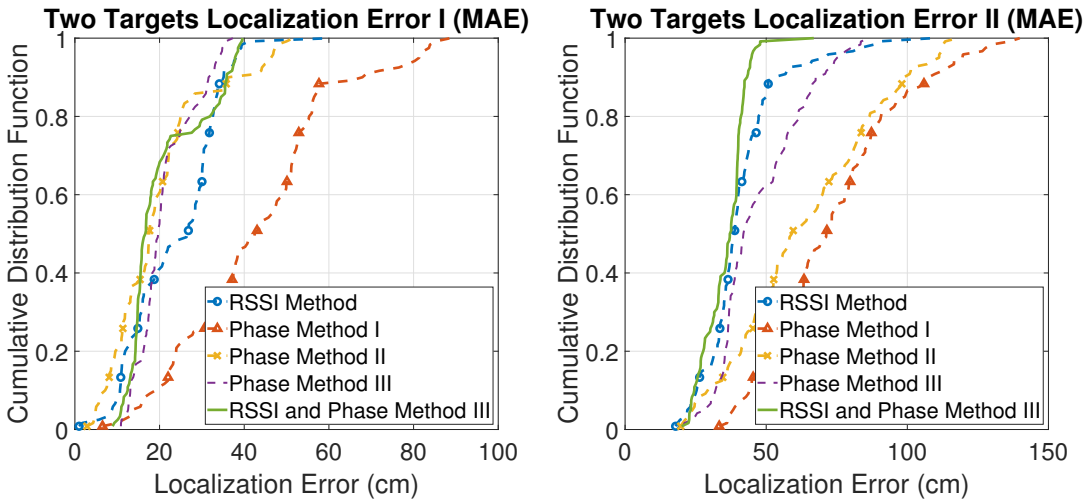

Figure 5.13: CDF of the localization error of 2 targets using k-Means for clustering and the 5th power for scaling.

the limitations of the current signal model. Future research should investigate non-linear signal models that consider scattering and occlusion between targets.

In conclusion, the shadowing effect caused by the targets is a critical factor. The RSSI Method and Phase Methods II and III utilize this information effectively, outperforming Phase Method I, which does not account for it. Additionally, the combination of RSSI and phase measurements in the fused methods leads to better results than using either measurement alone. Specifically, the combination improves the RSSI Method about 40%, 13% and 28% in the one target, two targets and three targets localization scenario, respectively.

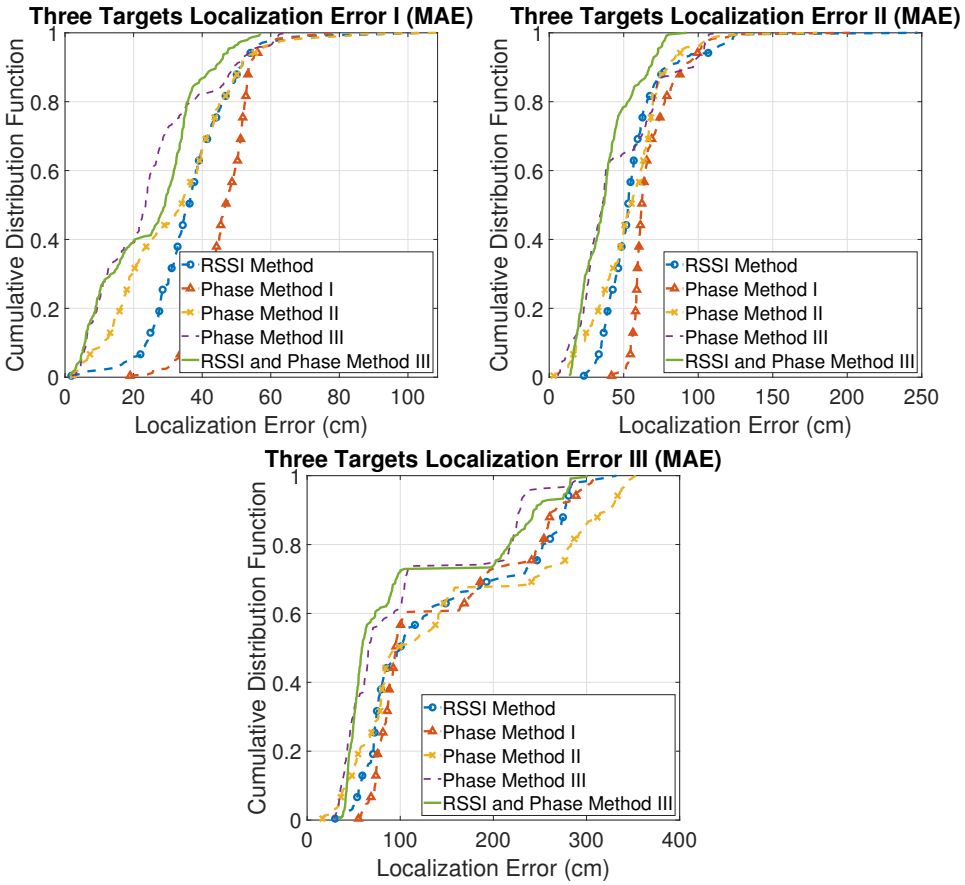

Figure 5.14: CDF of the localization error of 3 targets using k-Means for clustering and the 5th power for scaling.

Chapter 6

Conclusions

6.1 Conclusion

This work addressed the challenging problem of device-free localization (DFL) of multiple static humans in indoor environments. It presented two DFL methods and introduced a practical technique for combining multiple methods to enhance performance.

Through real world experiments, it was shown that both proposed methods show comparable results with prior art. Especially, the Phase Method with Read Rate can even outperform previous RSSI based methods in certain scenarios. Thus, it becomes evident that phase measurements and read rate can offer substantial information about the sensed environment and should not be overlooked.

Moreover, the proposed fusion technique greatly improved localization and produced remarkable results. It gives a simple way of utilizing both the RSSI, phase and read rate measurements and thus exploiting all the available information the RFID technology offers. Through all scenarios, it provided better accuracy than the combined methods individually and produced clearer images with better discernible targets and less artifacts. All these improvements come without sacrificing real time operation.

However, the multipath modeling is a very complex task and needs further improvement, as it is clear from the average performance of the Phase Method with RF propagation. As the number of targets increases, and inter-target reflections become more prevalent, the real environment deviates from the reflection model presented. The presence of multiple targets introduces greater non-linearity which the linear models can not tackle effectively. Therefore, non-linear models need to be developed to better capture the real environment conditions.

6.2 Future Work

Device-free localization (DFL) using passive RFID technology is both feasible and promising, but further research is needed to enhance its reliability, practicality, and energy efficiency.

The resolution of localization can be significantly improved by increasing the number of passive RFID tags. The low cost of these tags allows for the deployment of many around the sensed area, effectively increasing the number of antennas. This increase in spatial diversity, combined with the frequency diversity of the reader, enables more accurate localization of multiple targets.

The non-linearity introduced by multiple targets greatly reduces localization performance, and current linear models struggle to address this issue. To overcome this, new models that account for non-linearity are needed. Data-driven methods, particularly those involving deep learning, show promise in this area. Recent research has demonstrated the potential of autoencoder architectures to extract valuable information from sensor measurements, which can then be used to train classifiers for improved localization.

Power consumption is another critical aspect of DFL. Although RFID tags are batteryless, the readers consume about 1 watt of power, which is substantial. To make the system more energy-efficient, a multistatic setup can be employed. Deploying a large number of wireless illuminators distributed throughout the space can significantly reduce power consumption and enable sensing over larger areas.

Finally, while static target localization is more challenging, it does not fully represent real-life scenarios. Therefore, extending these methods to moving target localization is essential. Incorporating tracking and filtering algorithms can help monitor the movements of multiple targets, making the system more applicable to dynamic environments.

In summary, while passive RFID technology holds great promise for device-free localization, advancements in resolution, non-linearity modeling, energy efficiency, and the ability to track moving targets are necessary to fully realize its potential.

Appendix A

Localization images from all tested positions

1. One Target Localization Images

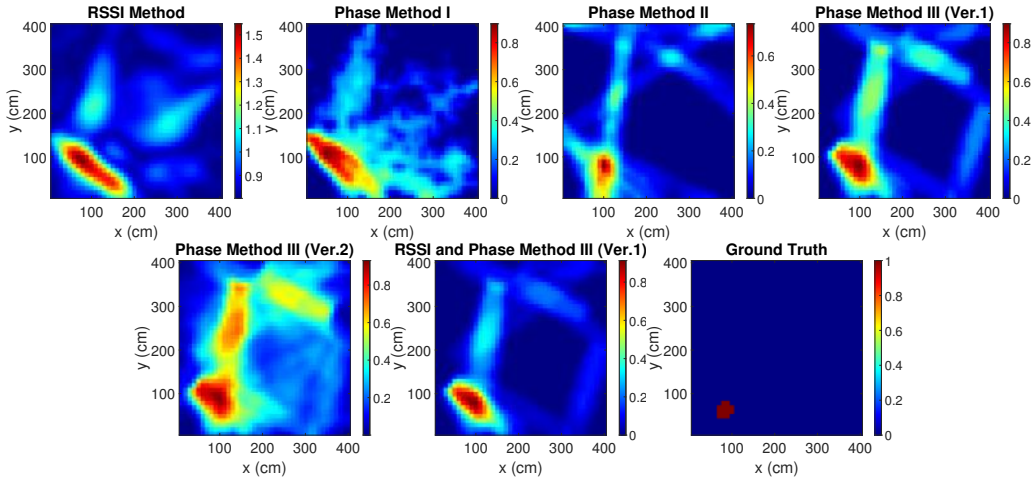

Figure A.1: Location 1

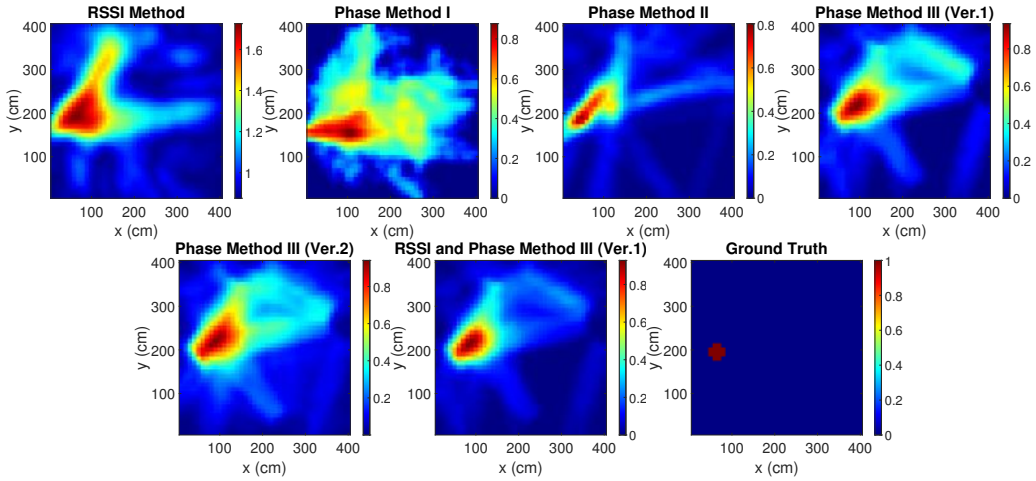

Figure A.2: Location 2

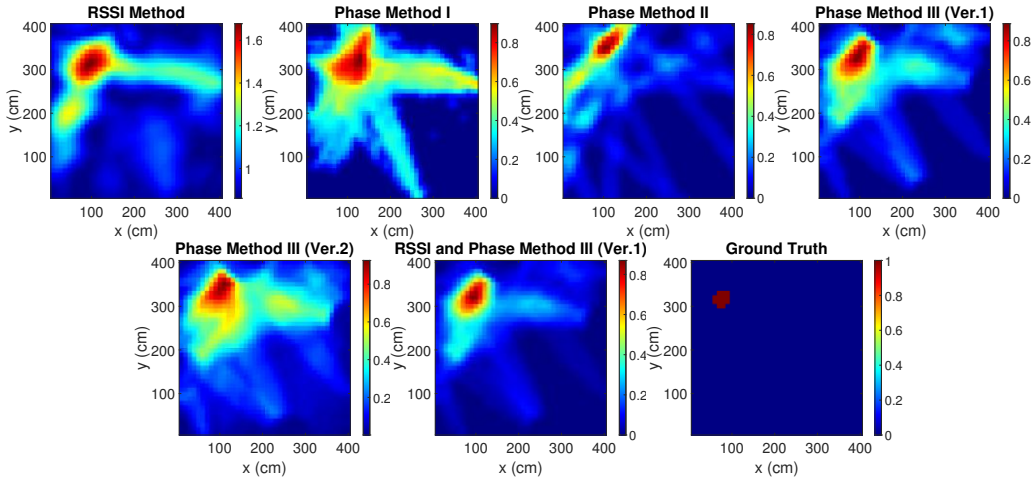

Figure A.3: Location 3

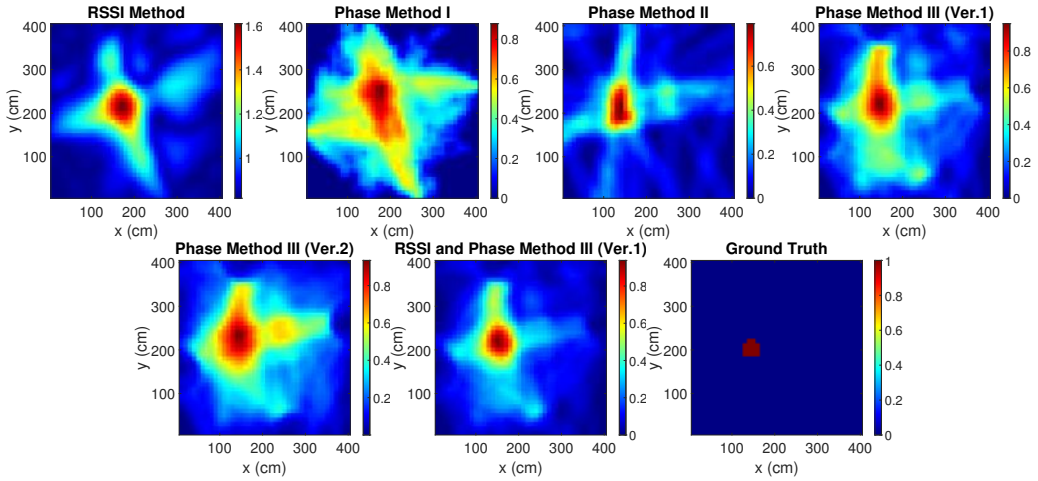

Figure A.4: Location 4

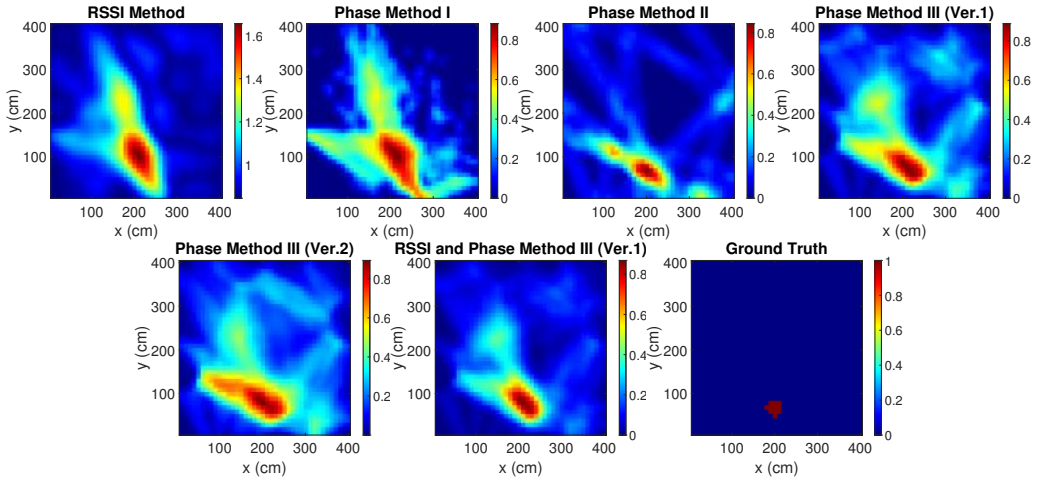

Figure A.5: Location 5

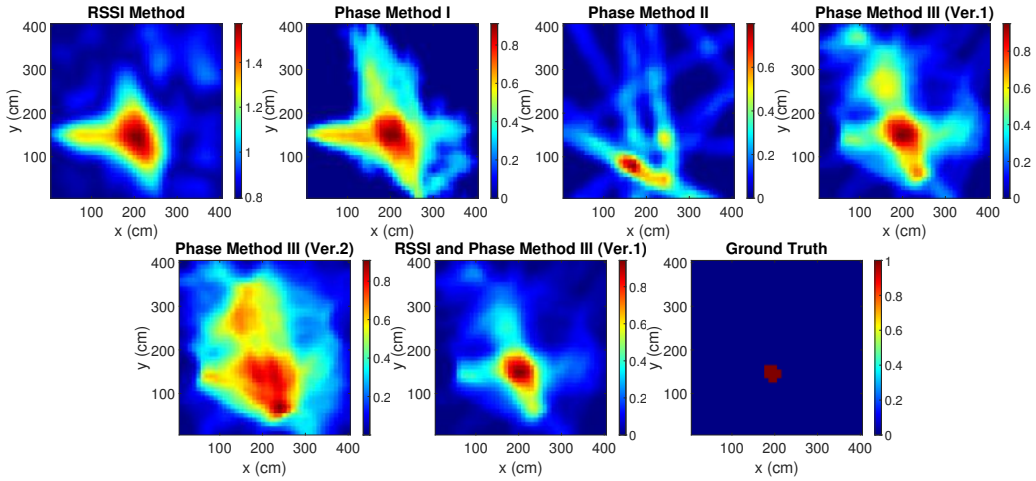

Figure A.6: Location 6

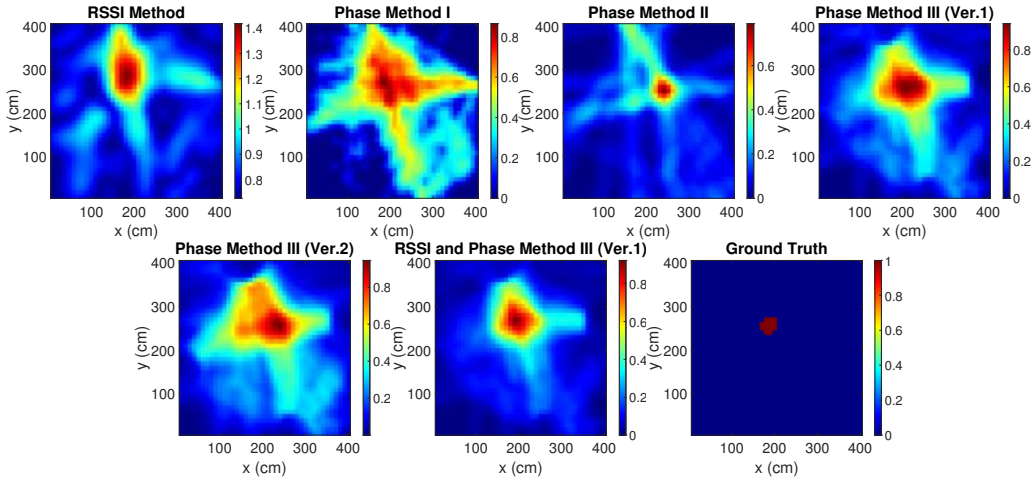

Figure A.7: Location 7

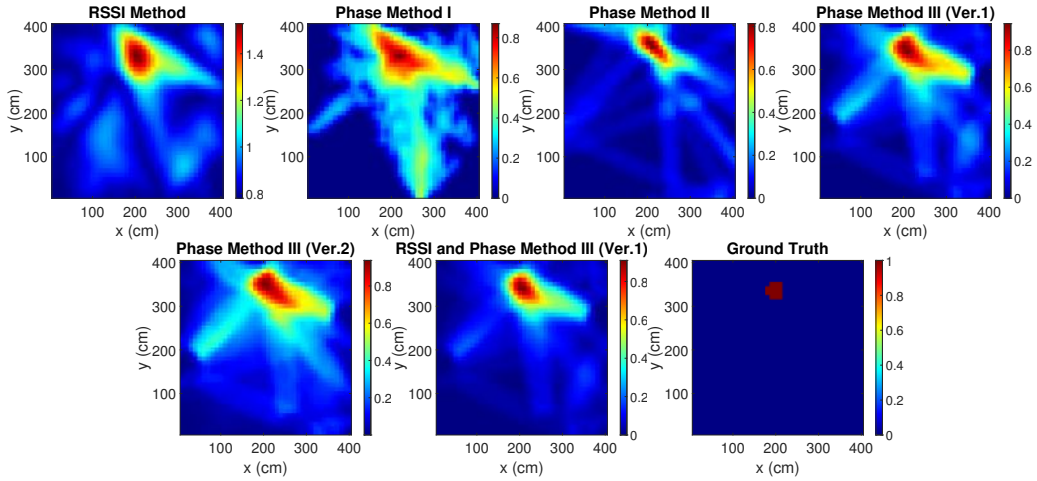

Figure A.8: Location 8

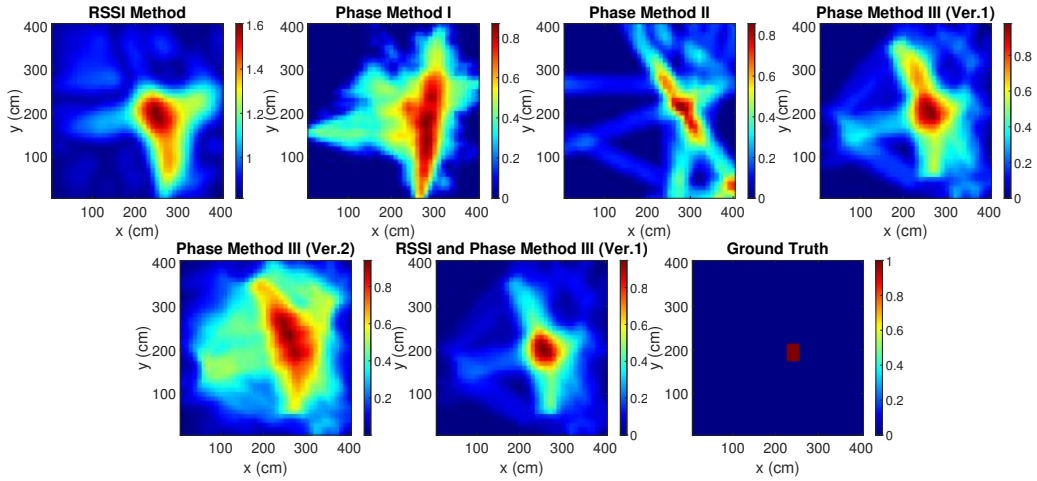

Figure A.9: Location 9

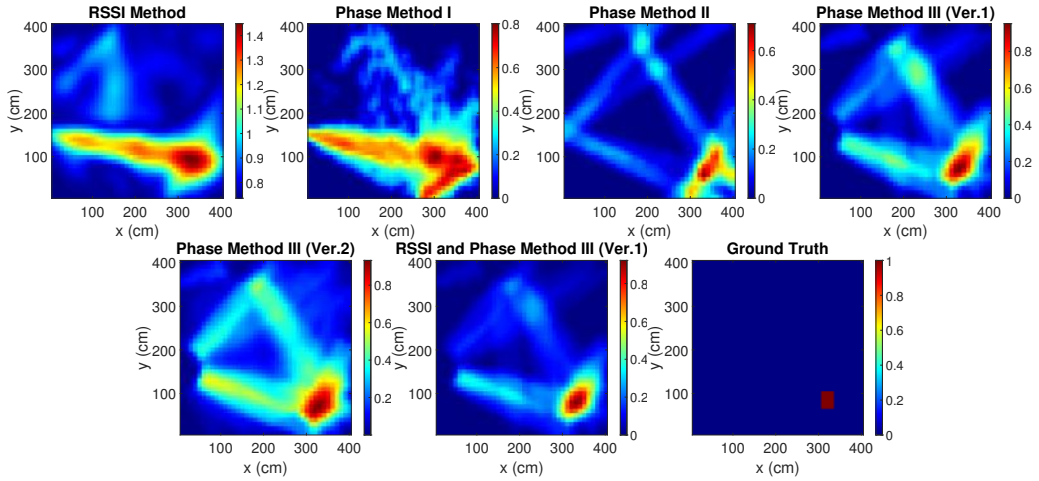

Figure A.10: Location 10

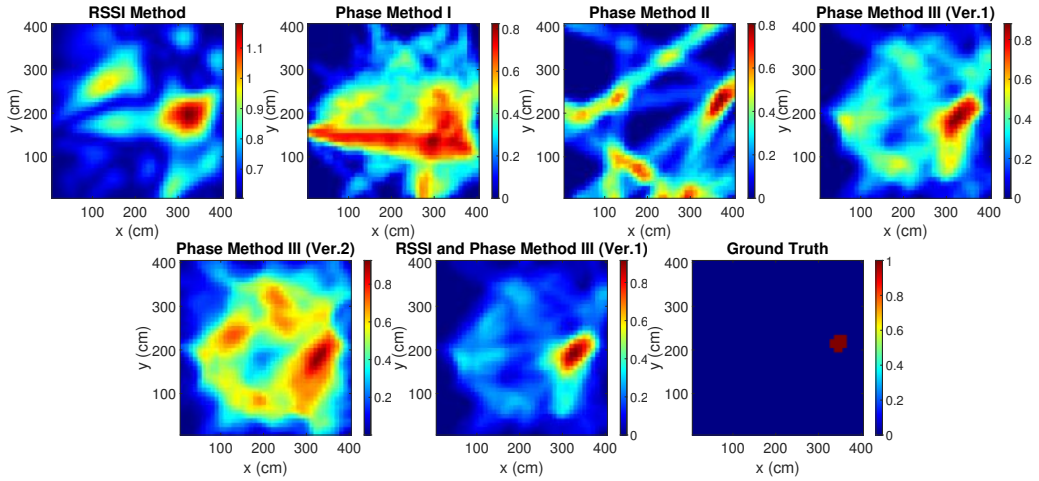

Figure A.11: Location 11

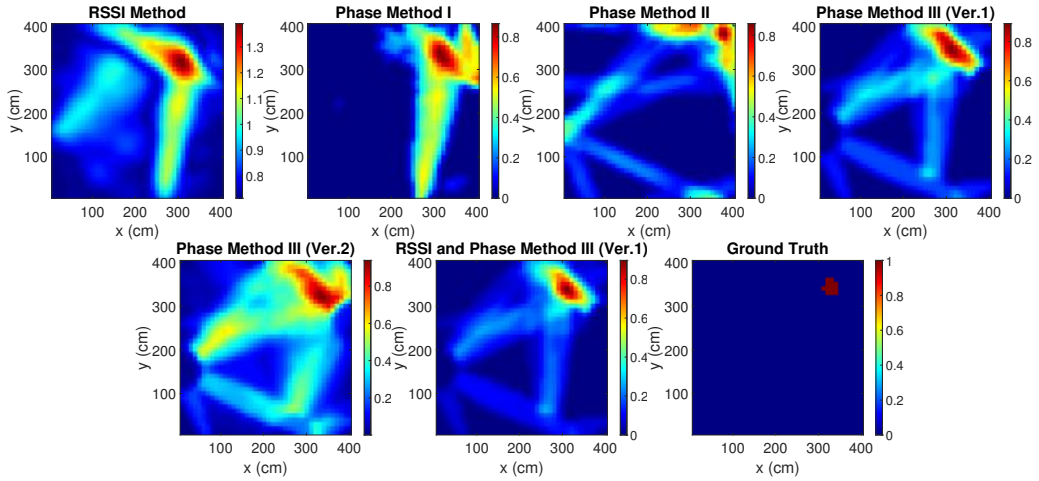

Figure A.12: Location 12

2. Two Targets Localization Images

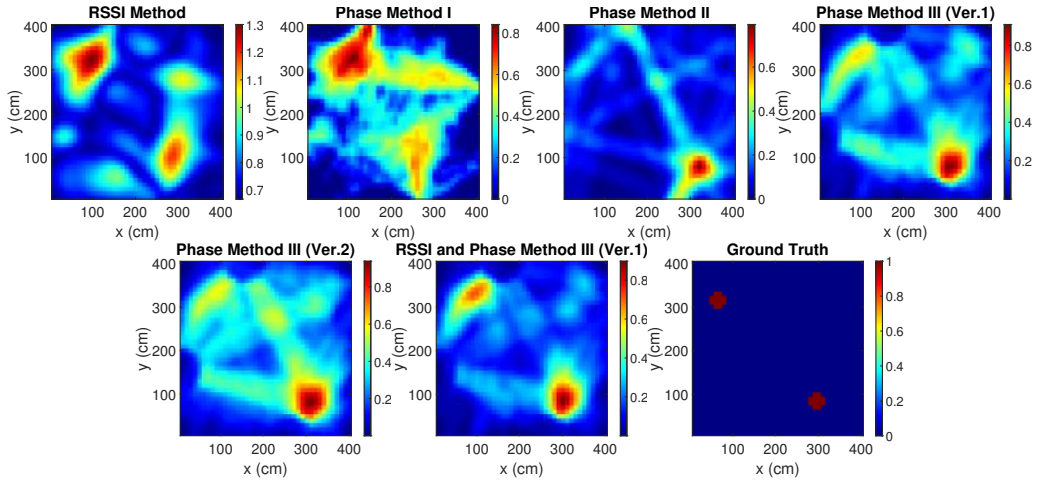

Figure A.13: Location 1

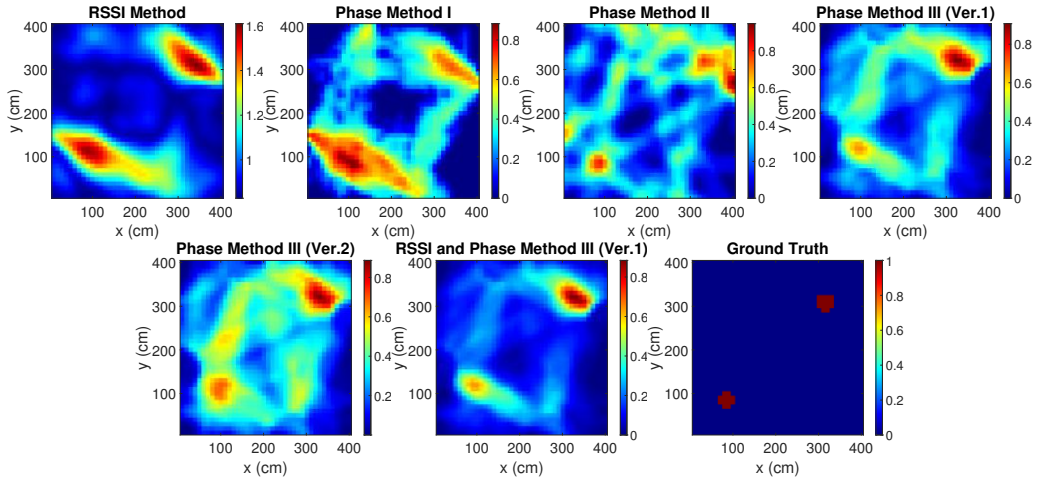

Figure A.14: Location 2

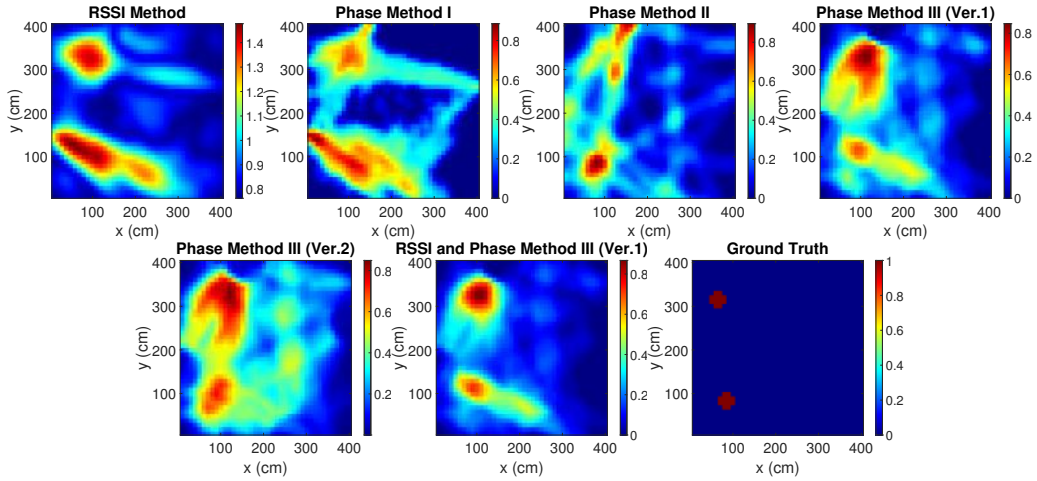

Figure A.15: Location 3

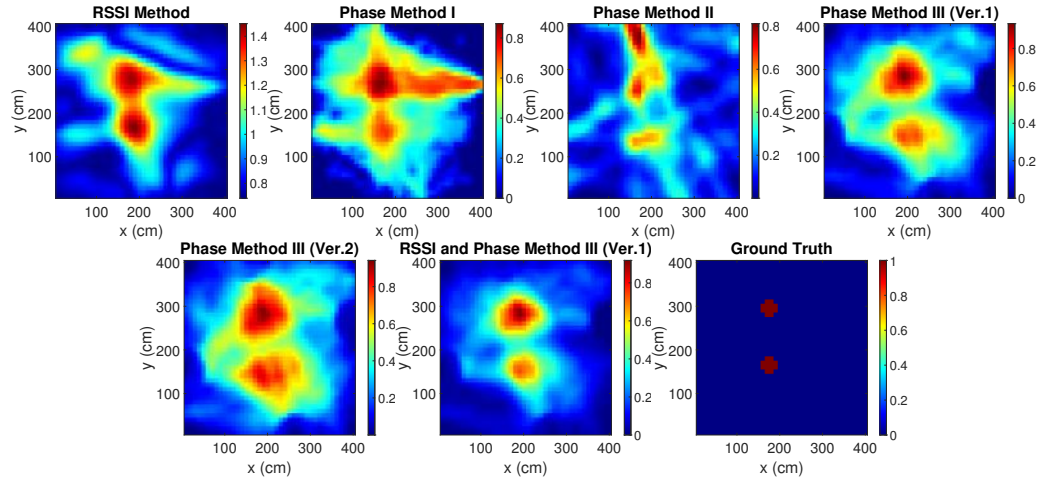

Figure A.16: Location 4

3. Three Targets Localization Images

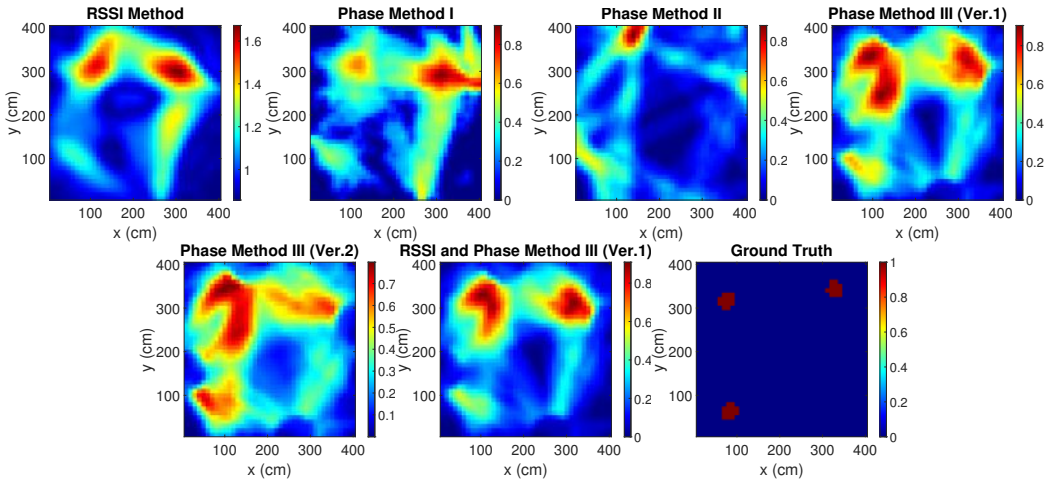

Figure A.17: Location 1

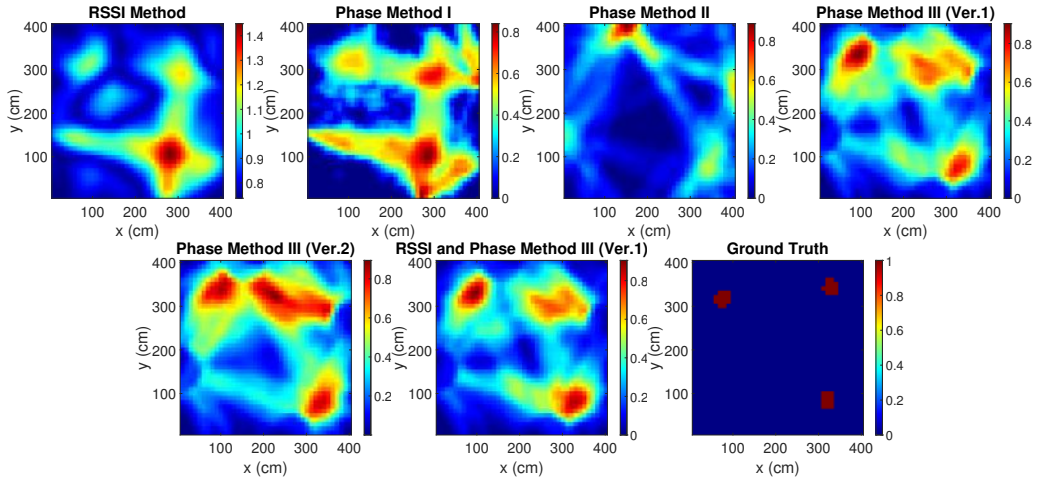

Figure A.18: Location 2

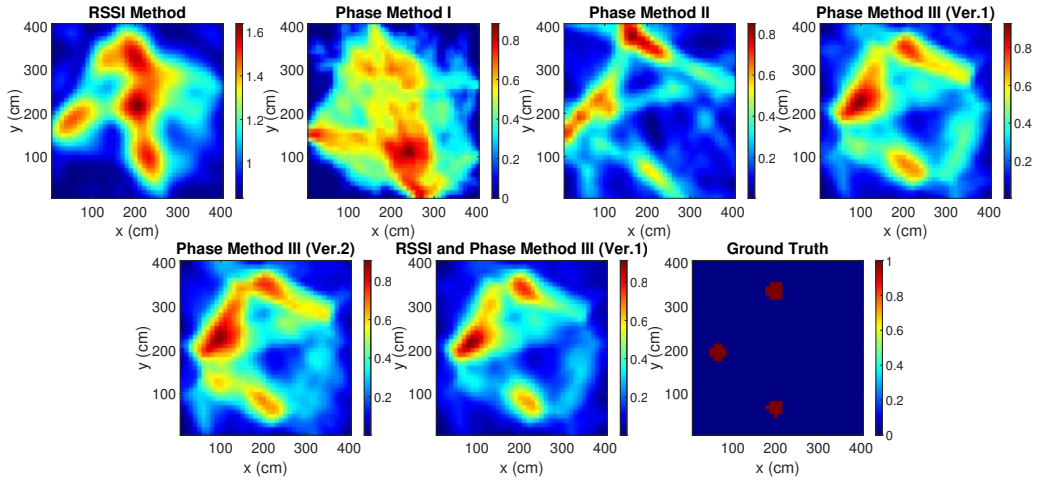

Figure A.19: Location 3

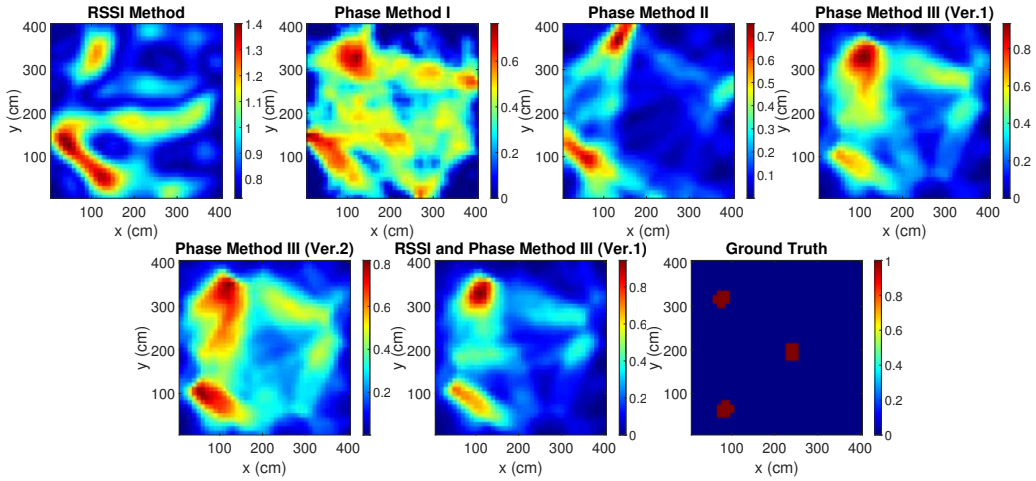

Figure A.20: Location 4

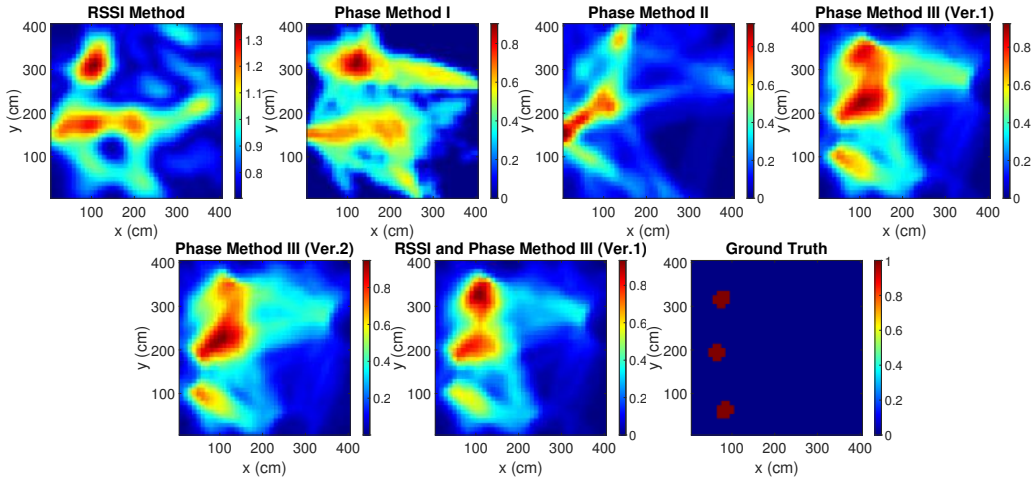

Figure A.21: Location 5

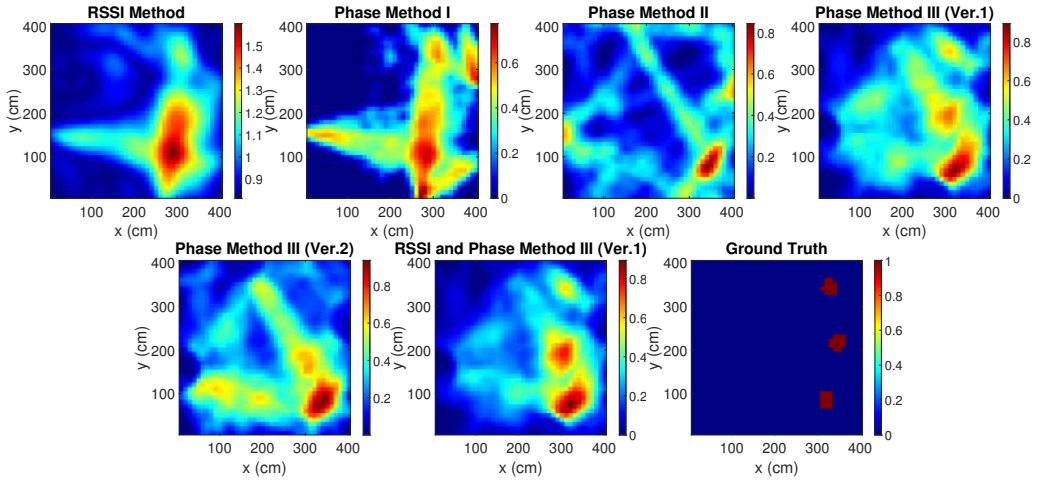

Figure A.22: Location 6

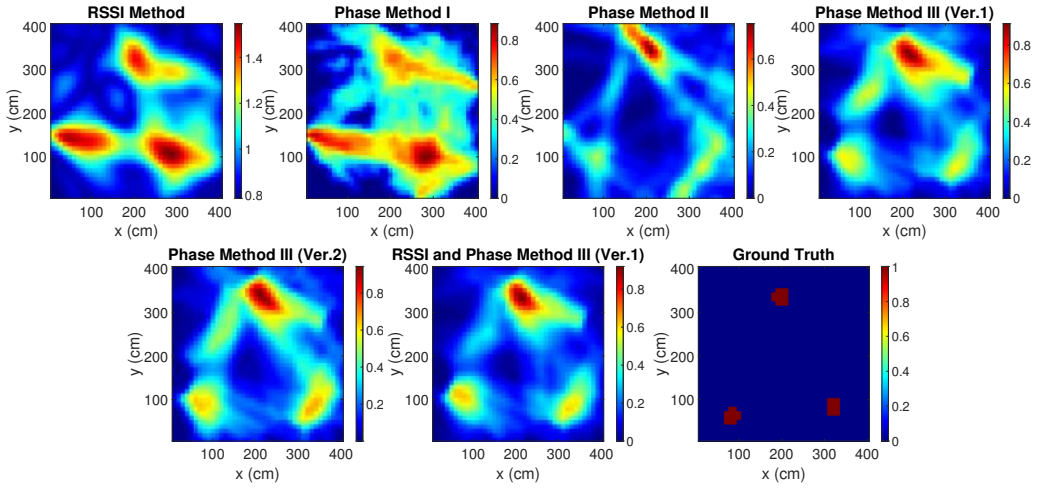

Figure A.23: Location 7

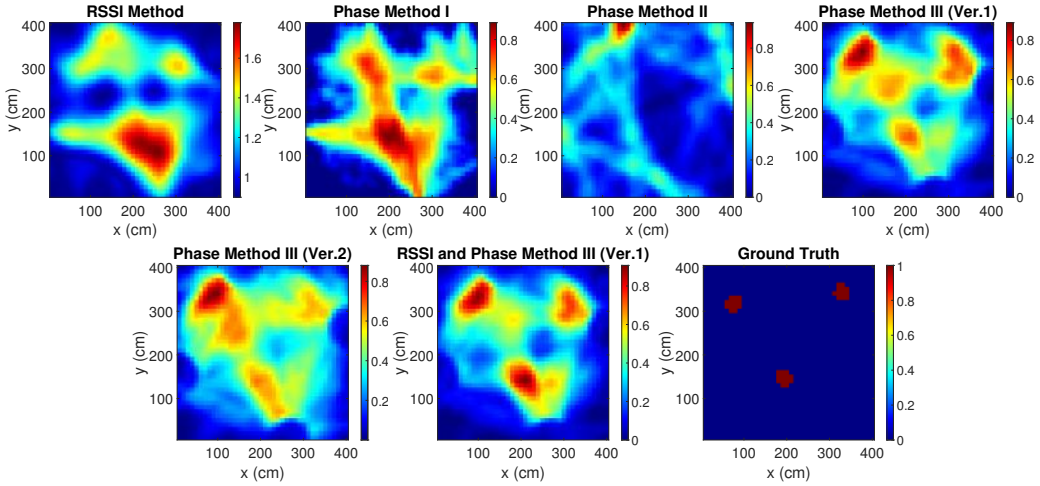

Figure A.24: Location 8

Bibliography

[1] A. Kleniatis, A. G. Dimitriou, and A. Bletsas, "Device-free Localization of Multiple Humans with Passive RFID and Joint RSSI-Phase Techniques," in *IEEE RFID 2024*, Boston, U.S.A, Jun. 2024.

[2] K. Joshi, D. Bharadia, M. Kotaru, and S. Katti, "WiDeo: fine-grained device-free motion tracing using RF backscatter," in *Proceedings of the 12th USENIX Conference on Networked Systems Design and Implementation*. USA: USENIX Association, 2015, p. 189–204.

[3] Y. Kilic, H. Wymeersch, A. Meijerink, M. J. Bentum, and W. G. Scanlon, "Device-Free Person Detection and Ranging in UWB Networks," *IEEE J. Sel. Topics Signal Process.*, vol. 8, no. 1, pp. 43–54, 2014.

[4] J. Wilson and N. Patwari, "Radio Tomographic Imaging with Wireless Networks," *IEEE Trans. Mobile Comput.*, vol. 9, no. 5, pp. 621–632, 2010.

[5] Y. Ma, B. Wang, X. Gao, and W. Ning, "The Gray Analysis and Machine Learning for Device-Free Multitarget Localization in Passive UHF RFID Environments," *IEEE Trans. Ind. Informat.*, vol. 16, no. 2, pp. 802–813, 2020.

[6] Y. Ma, Y. Zhang, B. Wang, and W. Ning, "SCLA-RTI: A Novel Device-Free Multi-Target Localization Method Based on Link Analysis in Passive UHF RFID Environment," *IEEE Sensors J.*, vol. 21, no. 3, pp. 3879–3887, 2021.

[7] H. Fu, Y. Ma, X. Gong, X. Zhang, B. Wang, W. Ning, and X. Liang, "Device-Free Multitarget Localization With Weighted Intersection Mul-

tidimensional Feature for Passive UHF RFID," *IEEE Sensors Journal*, vol. 22, no. 7, pp. 7300–7310, 2022.

[8] Y. Zhao and N. Patwari, "Demo abstract: Histogram distance-based radio tomographic localization," in *ACM/IEEE International Conference on Information Processing in Sensor Networks (IPSN)*, 2012, pp. 129–130.

[9] Y. Zhao, N. Patwari, J. M. Phillips, and S. Venkatasubramanian, "Radio tomographic imaging and tracking of stationary and moving people via kernel distance," in *ACM/IEEE International Conference on Information Processing in Sensor Networks (IPSN)*, 2013, pp. 229–240.

[10] G. Xu, P. Sharma, X. Hui, and E. C. Kan, "3-D Indoor Device-Free Object Detection by Passive Radio Frequency Identification," *IEEE Trans. Instrum. Meas.*, vol. 70, pp. 1–13, 2021.

[11] G. Xu, P. Sharma, D. L. Hysell, and E. C. Kan, "Indoor Object Sensing Using Radio-Frequency Identification With Inverse Methods," *IEEE Sensors J.*, vol. 22, no. 12, pp. 11 336–11 344, 2022.

[12] L. Ma, M. Liu, H. Wang, Y. Yang, N. Wang, and Y. Zhang, "WallSense: Device-Free Indoor Localization Using Wall-Mounted UHF RFID Tags," *Sensors*, vol. 19, no. 1, 2019.

[13] J. Wang, J. Xiong, H. Jiang, X. Chen, and D. Fang, "D-watch: Embracing "Bad" Multipaths for Device-free Localization with COTS RFID Devices," *IEEE/ACM Trans. Netw.*, vol. 25, no. 6, pp. 3559–3572, 2017.

[14] B. Mager, P. Lundrigan, and N. Patwari, "Fingerprint-Based Device-Free Localization Performance in Changing Environments," *IEEE J. Sel. Areas Commun.*, vol. 33, no. 11, pp. 2429–2438, 2015.

[15] W. Ning, Y. Ma, and X. Liang, "One for More: Sparse Group Lasso for Multitarget Device-Free Localization With Single-Target Fingerprint Database Under RFID System," *IEEE Sensors Journal*, vol. 23, no. 15, pp. 17 510–17 523, 2023.

[16] S. Nannuru, Y. Li, Y. Zeng, M. Coates, and B. Yang, "Radio-Frequency Tomography for Passive Indoor Multitarget Tracking," *IEEE Trans. Mobile Comput.*, vol. 12, no. 12, pp. 2322–2333, 2013.

[17] C. Xu, B. Firner, R. S. Moore, Y. Zhang, W. Trappe, R. Howard, F. Zhang, and N. An, "SCPL: indoor device-free multi-subject counting and localization using radio signal strength," in *Proceedings of the 12th International Conference on Information Processing in Sensor Networks*. Association for Computing Machinery, 2013, p. 79–90.

[18] A. Tzitzis, A. R. Chatzistefanou, S. Megalou, S. Siachalou, T. Yioultsis, and A. G. Dimitriou, "Device-free Human Tracking Exploiting Phase Disturbances and Particle Filters," in *Proc. IEEE RFID*, 2022, pp. 126–131.

[19] L. Li, C. Guo, Y. Liu, L. Zhang, X. Qi, Y. Ren, B. Liu, and F. Chen, "Accurate Device-Free Tracking Using Inexpensive RFIDs," *Sensors*, vol. 18, p. 2816, 08 2018.

[20] Y.-H. Su, J. Ren, Z. Qian, D. Fouhey, and A. Sample, "TomoID: A Scalable Approach to Device Free Indoor Localization via RFID Tomography," in *Proc. IEEE Int. Conf. on Computer Communications (Infocom)*, 2023, pp. 1–10.

[21] B. Wagner, D. Timmermann, G. Ruscher, and T. Kirste, "Device-free user localization utilizing artificial neural networks and passive RFID," in *Ubiquitous Positioning, Indoor Navigation, and Location Based Service (UPINLBS)*, 2012, pp. 1–7.

[22] J. Wang, X. Zhang, Q. Gao, H. Yue, and H. Wang, "Device-free wireless localization and activity recognition: A deep learning approach," *IEEE Trans. Veh. Technol.*, vol. 66, no. 7, pp. 6258–6267, 2017.

[23] M. Leigsnering, F. Ahmad, M. G. Amin, and A. M. Zoubir, "Compressive sensing based specular multipath exploitation for through-the-wall radar imaging," in *Proc. IEEE Int. Conf. Acoust. Speech Signal Process. (ICASSP)*, Oct. 2013, pp. 6004–6008.

[24] S. Peppas, E. Giannelos, G. Vougioukas, and A. Bletsas, "Where is the Wall? Radar Imaging-Based Narrowband RFID and Reflector Localization," in *Proc. IEEE RFID*, 2022, pp. 144–149.

[25] A. Goldsmith, *Wireless Communications*. New York, NY, USA: Cambridge University Press, 2005.

[26] E. Candes and T. Tao, "Decoding by linear programming," *IEEE Trans. Inf. Theory*, vol. 51, no. 12, pp. 4203–4215, 2005.

[27] E. Candès, J. Romberg, and T. Tao, "Stable signal recovery from incomplete and inaccurate measurements," *Communications on Pure and Applied Mathematics*, vol. 59, Oct. 2006.